

Kartezio: Evolutionary Design of Explainable Pipelines for Biomedical Image Analysis

Kévin Cortacero¹, Brienne McKenzie¹, Sabina Müller¹, Roxana Khazen¹, Fanny Lafouresse¹,
Gaëlle Corsaut¹, Nathalie Van Acker², François-Xavier Frenois², Laurence Lamant², Nicolas
Meyer³, Béatrice Vergier^{4,5}, Dennis G. Wilson⁶, Hervé Luga⁶, Oskar Stauffer⁷, Michael L. Dustin⁷,
Salvatore Valitutti^{1,2*#} and Sylvain Cussat-Blanc^{6*#}

¹INSERM UMR1037, CNRS UMR5071, Centre de Recherche en Cancérologie de Toulouse (CRCT),
Université de Toulouse III-Paul Sabatier, 31037 Toulouse, France

²Department of Pathology, Institut Universitaire du Cancer-Oncopole de Toulouse, 31059 Toulouse, France

³Department of Dermatology, Institut Universitaire du Cancer-Oncopole de Toulouse, 31059 Toulouse,
France

⁴Service de Pathologie CHU de Bordeaux

⁵Equipe INSERM UMR1053 -UMR BaRITOn (Eq 3), Université de Bordeaux

⁶University of Toulouse - Institut de Recherche en Informatique de Toulouse (IRIT)
Centre National de la Recherche Scientifique (CNRS) UMR5505,
Artificial and Natural Intelligence Toulouse Institute

⁷Kennedy Institute of Rheumatology, Nuffield Department of Orthopedics, Rheumatology
and Musculoskeletal Sciences, The University of Oxford, Oxford, UK

Abstract | An unresolved issue in contemporary biomedicine is the overwhelming number and diversity of complex images that require annotation, analysis and interpretation. Recent advances in Deep Learning have revolutionized the field of computer vision, creating algorithms that compete with human experts in image segmentation tasks. Crucially however, these frameworks require large human-annotated datasets for training and the resulting models are difficult to interpret. In this study, we introduce *Kartezio*, a modular Cartesian Genetic Programming based computational strategy that generates transparent and easily interpretable image processing pipelines by iteratively assembling and parameterizing computer vision functions. The pipelines thus generated exhibit comparable precision to state-of-the-art Deep Learning approaches on instance segmentation tasks, while requiring drastically smaller training datasets, a feature which confers tremendous flexibility, speed, and functionality to this approach. We also deployed *Kartezio* to solve semantic and instance segmentation problems in four real-world Use Cases, and showcase its utility in imaging contexts ranging from high-resolution microscopy to clinical pathology. By successfully implementing *Kartezio* on a portfolio of images ranging from subcellular structures to tumoral tissue, we demonstrated the flexibility, robustness and practical utility of this fully explicable evolutionary designer for semantic and instance segmentation.

#Co-senior authors

*Corresponding authors: salvatore.valitutti@inserm.fr and sylvain.cussat-blanc@irit.fr

Introduction

Contemporary imaging techniques in biology and medicine produce a tremendous quantity of images, which must be analyzed to provide meaningful interpretations of biological and clinical processes. The scale, context, and resolution of such images is highly variable, ranging from super-resolution and electron microscopy in biology to whole-tissue imaging in clinical pathology. Generating “actionable intelligence” from such imaging data, using either human or automated analysis of images, requires quantitative knowledge extraction [1]. The bottleneck of the knowledge extraction process has historically been the human power required for image evaluation, annotation, and interpretation, all of which can be time-consuming, prone to inter-human variability, and subject to error. Moreover, human nature imposes a subjective framework of reasoning that can affect the overall objectivity of the knowledge extraction process and the subsequent validation or invalidation of a given hypothesis. The development of sophisticated automated image analysis pipelines that preserve the nuances of human insight, while circumventing the abovementioned limitations, is a formidable challenge in contemporary biomedicine.

To keep pace with the development of increasingly sophisticated imaging techniques, engineers and researchers have designed a variety of image processing filters and pipelines that assist experimentalists and clinicians in extracting quantitative information from their digital images. Nevertheless, filters and pipelines need a certain level of expertise to be used optimally. Artificial Intelligence (**AI**) and more specifically Deep Learning (**DL**) approaches have since provided a great step forward in image processing and revolutionized the field of computer vision (**CV**). This is particularly evident in tasks such as Semantic Segmentation (**SS**), which clusters together parts of an image belonging to the same object class, and Instance Segmentation (**IS**) a complex task that additionally involves the demarcation of overlapping or interacting objects even if they belong to the same class. AI was proven to be competitive with human expertise in medical image analysis within the fields of cardiology, dermatology, ophthalmology, radiology and pathology among others [2, 3]. To date, these approaches have primarily been based on artificial Deep Neural Networks (**DNNs**), which are conceived to work at the pixel level to generate filters and pipelines from scratch without building on previous human knowledge and experience. This requires huge computational efforts to provide satisfactory solutions. DNNs are composed of thousands of simple computational units, the neurons, which are connected in a complex network of weighted interactions[4]. Designing the architecture of such a network is a key step before training. Because the subsequent training of an DNN to solve a given task requires the optimization of millions of parameters, DNNs require huge computational efforts to provide satisfactory solutions. Despite important advances in eXplainable AI (**XAI**)[5, 6], DNNs have generally been difficult for humans to analyze and interpret, leading to the definition of these models as “black-boxes”[5]. As such, there is substantial interest in developing more explainable “white-box” methods to complement existing DNN approaches in medical and biological image analysis.

Herein, we propose an innovative approach to image analysis that tackles the important challenges described above while remaining fully explainable and interpretable to humans. Our approach, named “Kartezio”, is based on the evolutionary design of pipelines assembled from pre-existing human-engineered filters. This is accomplished by using a specific type of Genetic Programming (**GP**) [7] algorithm, known as Cartesian Genetic Programming (**CGP**) [8-10], to generate image processing pipelines [11, 12]. As a case

study for this powerful approach, we deployed Kartezio to solve different IS and SS challenges, thematically centered around the field of tumor immunotherapy.

Proposed by Miller in 1999 [10], CGP has been successfully used in multiple variants (Mixed Types, Recurrent, Self-Modifying, etc. as reviewed in [13]) for logical circuit generation[9], symbolic regression, agent control[14], neural architecture search[15, 16] and simple image processing tasks such as noise reduction[17] and SS[11, 12] but to date the application of this powerful approach to IS in biomedicine has been limited. By merging CGP-based IS with CV measures and classical unsupervised machine learning (**ML**), we designed a highly effective AI solution to extract quantitative information from immunofluorescent (**IF**) and immunohistochemical (**IHC**) images. Our CGP-based strategy is: (i) trainable on small datasets, (ii) transparent and interpretable by humans, and (iii) capable of integrating human knowledge. The strategy presented in this manuscript (summarized in **Extended Data Fig. 1**) represents a substantially new conceptual framework for the design of image processing pipelines, and offers a novel approach to tackle the challenge of image analysis in contemporary medical and biological sciences.

Results

Evolving programs for instance segmentation with CGP

GP is based on the artificial evolution of a population of syntactic graphs composed of mathematical functions that, when executed, process given inputs to produce an expected output[7]. While GP directly works on the optimization of syntactic graphs, CGP considers a specific encoding of this graph within an integer-based genome, also called genotype (**Fig. 1a-b**, see **Material and Methods**). In this paper, we developed a modular framework (called **Kartezio**) to expand CGP into IS tasks and to confer enhanced versatility to its application, thus revitalizing the CGP approach to iteratively evolve image segmentation pipelines (illustrated in **Extended Data Movie 1**) based on functions drawn from a pre-existing library. To this end, we first built a library of 42 functions specifically designed for IS (full library is provided in **Extended Data Table 1**). In addition, we introduced the notion of *non-evolvable nodes* which are functions not subjected to optimization of the syntactic graph (**Fig. 1c**). The objective of these two initial steps was to introduce human knowledge about the input images, expected outputs and, if requested, additional known operators into CGP-generated pipelines. With these adaptations, we re-invigorated the CGP paradigm to make it more versatile and introduced (i) non-evolvable preprocessing nodes to transform input images (e.g. transmission light images, fluorescent images, IHC tissue images, etc.) into the most appropriate format for the expected outcome, and (ii) appropriate endpoints (such as Watershed Transform[18, 19] or Circle Hough Transform[20]) which can strongly reduce the search space to perform IS, similarly to what is done in many current DNN-based methods[21-25]. Together the decoded genotype and the non-evolvable nodes will produce executable image processing pipelines (**Fig. 1d**).

In the next section, we compare our CGP approach to state-of-the-art DL techniques applied to cell IS within microscopy images.

Kartezio outperforms Mask R-CNN and StarDist and approaches Cellpose performance in instance segmentation tasks

To evaluate our CGP performance, we compared Kartezio to Cellpose[21], a recently released DL approach for IS in biology, as well as to two previously released approaches, Mask R-CNN[23] and StarDist[22]. The Cellpose algorithm used a generalist model trained on a dataset that contained over 70,000 segmented objects. The authors also generated a specialist model, trained on 89 images, for IS of *in vitro* cultured neurons[26] stained with phalloidin and DAPI and imaged using an epifluorescence microscope (individual channels from a representative image are displayed in **Extended Data Fig. 2a**). In our study, we used subsets of these 89 images (ranging from 1 to 89 images) to train Kartezio from scratch and subsequently evaluated its performance on a test dataset of 11 previously unseen images from the same study. The training and testing parameters are detailed in **Extended Data Table 2**.

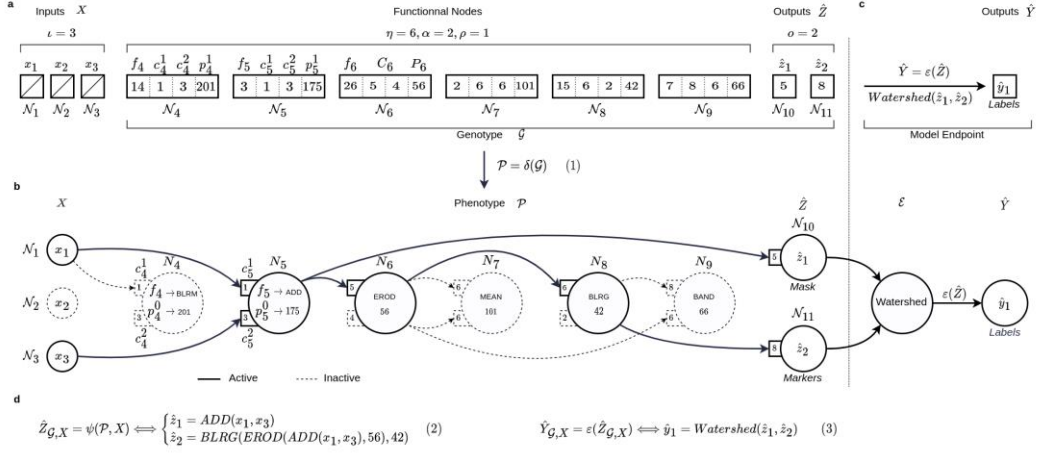


Fig. 1 | Architecture of Kartezio: a model for instance segmentation that extends CGP

a) The genome \mathcal{G} is a sequence of integers that are organized in genes. They are separated in two parts: i) the functional nodes ($\mathcal{N}_{4 \rightarrow 9}$) and ii) the outputs ($\mathcal{N}_{10 \rightarrow 11}$). The panel shows an arbitrary example composed of three entry channels ($\mathcal{N}_{1 \rightarrow 3}$), six functional nodes ($\mathcal{N}_{4 \rightarrow 9}$) and two outputs ($\mathcal{N}_{10 \rightarrow 11}$). **b)** The CGP graph \mathcal{P} decoded from the genome described in a) is shown. To obtain the active graph only the genes that are directly or indirectly connected to outputs are considered. **c)** The panel describes the last operation of the pipeline (Endpoint) that consists in the addition of a defined function that helps evolution to converge faster to a given solution. While the Endpoint is part of the evaluation of the genomes, it is not subjected to evolution and is chosen by the user depending on the task to solve. **d)** Functional program extracted from the active nodes of the graph.

Fig. 2a and **Extended Data Table 2** show the scores obtained on the 11-image test dataset after first training Kartezio on datasets of different sizes. Dotted lines indicate the results obtained by the other three methods as reported in Stringer *et al* [21], when trained on all 89 images. It is interesting to note that Kartezio frequently outperformed Mask R-CNN[23] and StarDist[22] even when trained on much smaller datasets (e.g. on average, Kartezio matched Mask R-CNN when trained on as few as 6 images, and matched StarDist when trained on only 3 images). This illustrates the exceptional capacity of Kartezio to extrapolate from a very small set of training images (a property known as “few-shot learning”) and yet achieve comparable or superior accuracy compared to state-of-the-art DL approaches. Our results also show that the best score obtained by Kartezio was 0.89, a value comparable to the reported best performance of Cellpose (0.91) (**Extended Data Table 2**).

The capacity of Kartezio to extrapolate from only a few training events was also evident when we compared the scores obtained on training subsets with those obtained on the 11-image test dataset. In this analysis, a score of 0 is optimal as it shows no decrease in accuracy when transitioning from the training to the test set. As shown in **Fig. 2b**, the difference of mean average precision between the training and test sets was close to 0 when only 9-10 images were used for training.

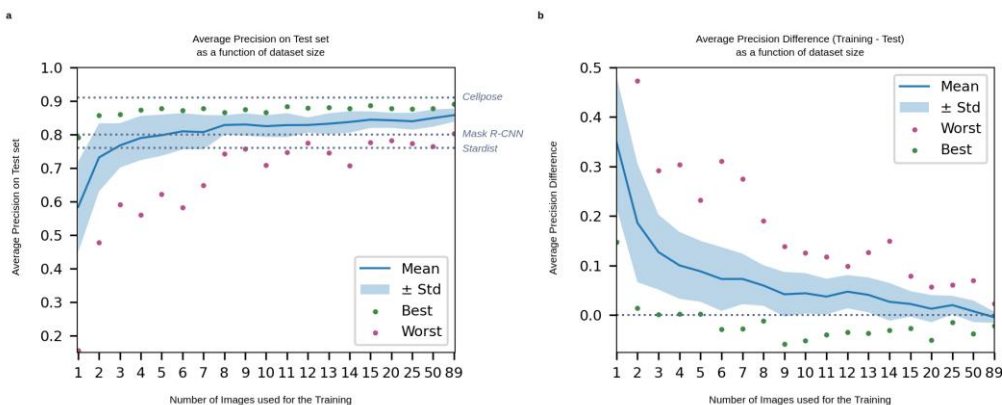


Fig. 2 | Kartezio achieves comparable precision to state-of-the-art deep learning approaches
Kartezio was trained on various numbers of images ranging from 1 to 89. Its performance on a previously unseen test set of 11 images was compared to results obtained by Cellpose, Mask-RCNN and StarDist (each trained on a set of 89 images). **a)** The plot shows the Average Precision (AP50) scores for the indicated number of images used for training Kartezio (data shown represent the mean \pm standard deviation of $n=35$ pipelines for the indicated number of training images). Dotted lines indicate the reported results obtained by each of the other three methods. **b)** The plot shows the average difference between scores obtained on the training image dataset and those obtained on the test image dataset (data shown represent the mean \pm standard deviation of $n=35$ pipelines for the indicated number of training images). The dotted line indicates an optimal difference of 0. Dots indicate the best (green) and worst (red) scores obtained by Kartezio for the indicated number of training images.

These data indicate that Kartezio generates pipelines of comparable precision to state-of-the-art DL approaches but with a drastic reduction in the size of the training dataset.

In the following sections of this article, we will present a portfolio of applications of Kartezio-based image analysis (three IS tasks and one SS task) at different scales (from nanometer-size extracellular particles to centimeter-size tumor nodules), conceptually centered around the theme of cytotoxic T lymphocyte (CTL)/tumor cell interactions in the context of tumor immunology. **Extended Data Table 3** outlines the key features of dataset preparation and analysis for the four different Use Cases in the portfolio. **Extended Data Table 4** summarizes the model parameters for each Use Case and **Extended Data Table 5** includes the fitness scores (min, max, and mean) for testing and training datasets. All four Use Cases utilize the same default library of 42 functions (**Extended Data Table 1**) and the same hyper-parameters (e.g. number of functional nodes, mutation rates, etc.). Of note, the library and hyper-parameters can be still adapted by the user if requested. We have also included examples of possible post-segmentation analyses for each Use Case (performed after image segmentation by Kartezio and listed in **Extended Data Table 3**); these are for illustrative purposes and can be modified to answer different experimental questions without changing the function of Kartezio.

Use Case 1 - Multi-molecular scale: detecting and measuring CTL-derived extracellular particles

Recent studies revealed that the fight between CTLs and tumor target cells is not limited to lytic synapses (specialized cell-cell contact areas where cytotoxic lytic granules are secreted from killer CTLs [27, 28]) but also occurs via the release of extracellular aggregates of lytic components and additional bioactive molecules called Supra Molecular Attack Particles (SMAPs)[29, 30]. SMAPs are currently under investigation as potential

anti-cancer therapeutics and may represent a potent new tool in the arsenal of oncologists. It is therefore crucial to develop new methods to characterize these particles in order to better define their biological function and therapeutic potential. As individual CTL-derived SMAPs are small (~120nm in diameter, as detected by D-STORM imaging) [30], high-resolution imaging techniques are required for their visualization.

In a first application of Kartezio, we acquired high-resolution Total Internal Reflection Fluorescence Microscopy (**TIRFM**) images of particles released from human polyclonal CD8⁺ CTLs and stained with Alexa 647-conjugated wheat germ agglutinin (**WGA**; a red fluorescent probe that stains sialic acid and N-acetyl-glucosamine moieties of glycoproteins), and DiO (a green fluorescent lipophilic dye that stains hydrophobic lipid membranes); individual channels from a representative image are displayed in **Extended Data Fig. 2b**. The population of particles included WGA⁺ (*cyan*), DiO⁺ (*magenta*) and double positive particles (*lavender*) (**Fig. 3a**). The aim of this test paradigm was to determine if Kartezio could distinguish putative SMAP particles (WGA⁺DiO⁻) from a mixed population of extracellular particles and vesicles, and then to extract quantitative information about the different particle populations. Although conceptually simple, this Use Case enabled us to demonstrate the performance of Kartezio in the context of single-particle high-resolution imaging.

Using Kartezio, we created an automated procedure to perform IS, which permitted the subsequent identification of single- and double-positive particles and characterization of their features. For each channel, we first trained Kartezio on a dataset consisting of one manually-labelled image, split into quarters (the number of ROIs is indicated in **Extended Data Table 3**). Based on 35 training runs, Kartezio achieved an average AP50 score of 0.81 (± 0.038) and 0.79 (± 0.030) for the WGA and DiO channels respectively, with a maximum score of 0.87 and 0.84 for WGA and DiO respectively. To assess generalizability, all IS pipelines were then tested on a dataset of one manually-labelled previously unseen image, split into quarters. Under these test conditions, Kartezio achieved an average AP50 score of 0.73 (± 0.084) and 0.76 (± 0.091) for the WGA and DiO channels respectively, with a maximum score of 0.84 for WGA and 0.85 for DiO. These results are summarized in **Extended Data Table 5**.

For each channel, the best overall pipeline (based on test and training fitness scores) was then applied to an image cohort containing an additional 9 images of CTL-derived extracellular particles. For the WGA channel, the best overall pipeline had a training fitness score of 0.87 and a test fitness score of 0.84. For the DiO channel, the best overall pipeline had a training fitness score of 0.81 and a test fitness score of 0.85. **Fig. 3b** shows a representative example of cyan and magenta particle segmentation obtained with the best pipeline for each channel out of the 35 runs performed. In order to identify double-stained particles post-segmentation, the WGA and DiO instances previously detected using Kartezio were tested for matching using a pairing mechanism based on the Intersection over Union (**IoU**) metric (detailed in **Materials and Methods**). Instances detected in the WGA and DiO channels with the IoU score above a threshold of 0.05 were identified as double-positive instances. The entire process enabled the identification of three sets of particles: WGA⁺DiO⁻ (*cyan*), WGA⁻DiO⁺ (*magenta*), and WGA⁺DiO⁺ (*orange*) (**Fig. 3c**).

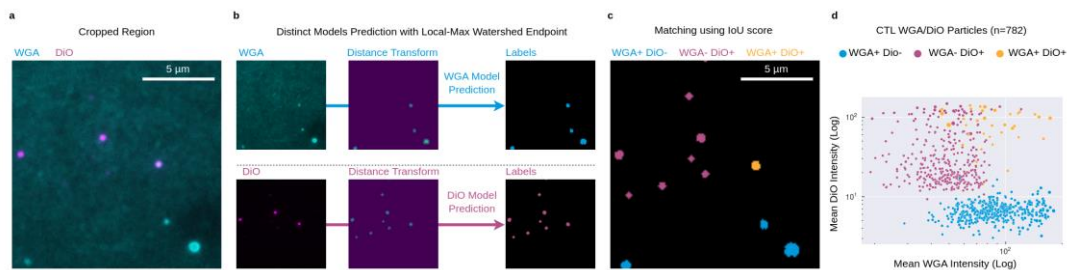


Fig. 3 | Analysis of extracellular particles using Kartezio-mediated instance segmentation
Use Case 1: CTL-derived extracellular particles stained with WGA and DiO were imaged using TIRFM. **a)** A typical cropped image depicting extracellular particles that were positive for either WGA (cyan), DiO (magenta) or both. **b)** The two images on the left depict the individual channels (WGA and DiO). For each channel, Kartezio generated a model for instance segmentation (arrows) leading to labels via the Local Max Watershed Endpoint. Each label corresponded to one instance (particle) in a given channel as shown. **c)** To begin the post-segmentation analysis, each label was classified as WGA⁺ (cyan), DiO⁺ (magenta) or WGA⁺DiO⁺ (gold), with matching evaluated on the basis of label overlap using the Intersection over Union (IoU) metric. **d)** Feature extraction from each instance involved quantification of particle size and mean fluorescence intensity (MFI). Individual dots represent WGA⁺ (cyan), DiO⁺ (magenta) and WGA⁺DiO⁺ double positive particles (gold) plotted on the basis of MFI. Dot size is proportional to the size of the particle mask corresponding to each instance.

From these datasets we could readily calculate the mean fluorescence intensity (MFI) and area of each instance as shown in **Fig. 3d**. The panel displays a scatterplot of WGA⁺DiO⁻ (cyan), WGA⁻DiO⁺ (magenta), and WGA⁺DiO⁺ particles (orange) released from CTLs. This analysis proved capable of distinguishing extracellular vesicles (WGA⁻DiO⁺ and WGA⁺DiO⁺ particles) from putative SMAPs, which were previously shown to be WGA⁺ but negative for lipophilic plasma membrane dyes[30].

Taken together, the above results show that Kartezio can successfully perform rapid and accurate IS of extracellular particles at a multi-molecular scale, providing access to further analysis of a statistically relevant number of events. It is important to note that the pipelines generated by a Kartezio can be exported to standard Python scripts (see **Extended Data Fig. 3**), which can be readily re-used on additional images acquired in comparable experimental conditions.

Use Case 2 - Sub-cellular scale: assessing the lytic arsenal of individual CTLs

To test Kartezio's performance on a larger scale, we assessed the capacity of Kartezio to automatically measure expression of various molecules within cells, in order to classify individual cells based on their molecular content. Here we focused on the CTL lytic arsenal by measuring the expression of various lytic granule components (e.g. perforin, granzyme B, and CD107a) in polyclonal human CTLs. Cells were stained with antibodies directed against CD45 (grayscale), perforin (magenta), granzyme B (yellow) and CD107a (cyan) (see **Extended Data Fig. 2c**). Staining for CD45, a molecule expressed on the surface of all hematopoietic lineage cells including CTLs, allowed Kartezio to delineate individual cells, while the other markers were subsequently used to score the CTL lytic arsenal during the post-segmentation analysis.

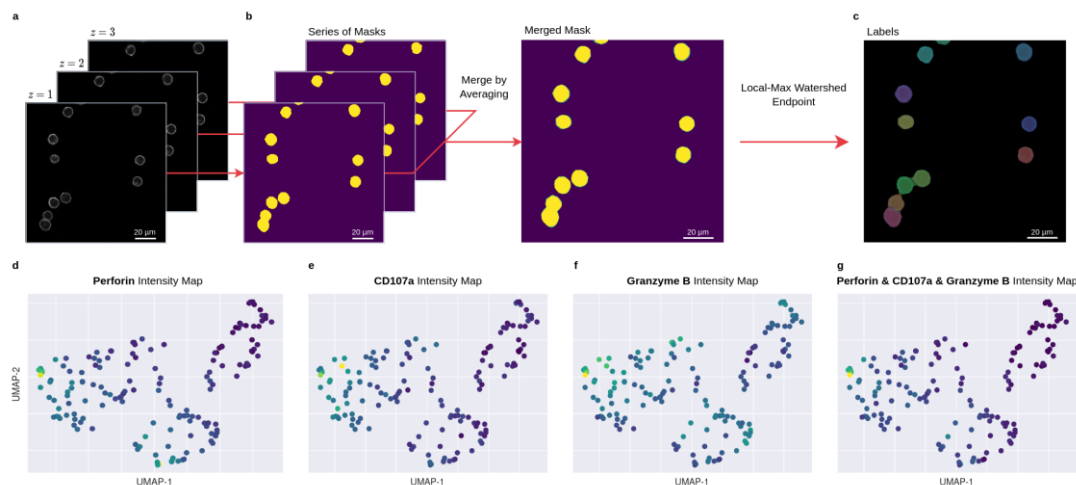


Fig. 4 | 3D analysis of lytic molecule content in individual CTLs within a polyclonal population

Use Case 2: Human polyclonal CD8⁺ T cells were stained with antibodies directed against CD45, perforin, granzyme B and CD107a (see **Extended Data Fig. 2c**). **a)** z-stacks of images in the CD45 channel were used as a 3D input to delimitate individual cells. **b)** Kartezio generated an instance segmentation pipeline that was sequentially applied to each layer of the z-stack to generate the corresponding mask. The masks were aggregated using an averaging operator. **c)** The application of the Local Max Watershed Endpoint allowed the generation of 2D labels. **d-f)** For the post-segmentation analysis, the MFI of perforin, granzyme B, and CD107a was calculated for each instance to derive a single feature vector for each cell. This vector was a composite of different quantitative readouts and integrated both individual and combined counts of positive pixels, sums of pixel fluorescence intensities, and average intensities measured in the different channels. Each cell was visualized on a 2D UMAP representation [31] based upon this composite feature vector. **g)** The same UMAP representation of merged lytic components.

For the initial analysis, we applied Kartezio to series of z-stacks containing CD45 staining only (**Fig. 4a**). To achieve this aim, we upgraded Kartezio to segment cells in 3D stacks to provide accurate 2D masks of each identified cell. Kartezio-generated pipelines were sequentially applied to each layer of the z-stack to produce initial Watershed masks of each z-stack. All the masks were merged with an averaging operator which allowed us to obtain the maximal area of the cells in the z-dimension (**Fig. 4b**). Local Max Watershed was applied to produce the IS masks of the cells (individual segments, **Fig. 4c**).

For this analysis, the training fitness was more stringent than in the previous analysis (AP with a threshold of 0.7 instead of 0.5) to avoid overfitting. The training dataset was limited to 5 images containing 45 cells, highlighting the aforementioned capacity of Kartezio to be trained for cell segmentation on a very small set of images. On 35 independent runs, Kartezio obtained an average score of 0.93 (± 0.064) on the training dataset (n=5 images with 45 cells) and 0.83 (± 0.029) on the test dataset (n=4 images containing 34 cells), with a maximum score of 1.000 during training and 0.89 during testing (results shown in **Extended Data Table 5**). The best overall pipeline had a score of 1.00 during training and 0.85 during testing.

After the individual cells were segmented using Kartezio's best pipeline, we measured staining of the three lytic granule components (perforin, granzyme B, and CD107a) in each z-section to derive a single feature vector for each cell. This vector was a composite of different quantitative readouts and integrated both individual and combined counts of positive pixels, sums of pixel fluorescence intensities, and average intensities measured in the different channels (see **Material and Methods**). Each cell was then positioned on the UMAP[31] based upon this composite feature vector. The gradient of expression of each

lytic granule component within cells of the whole population is shown in **Fig. 4d-f**. **Fig. 4g** shows the gradient of expression in the whole population for the three markers together.

Together these results underline the capacity of Kartezio to serve as a versatile tool for the analysis of molecular content in cells. Importantly, this function can be used more broadly to automatically assess staining intensities in a wide range of microscopy images, one of the most common tasks in image analysis in cell biology.

Use Case 3 - Cell-cell interface scale: discerning CTL/target cell lytic synapses within a mixed population of cells

In the next step of Kartezio's validation, we focused our analysis on lytic synapses, which are highly ordered structures that form when a CTL productively engages a target cell that expresses its cognate antigen[27, 28]. A CTL/target cell interaction that forms around a lytic synapse is known as a cell-cell "conjugate". Identifying a CTL/target cell conjugate is a complex task, which involves correctly identifying and demarcating different cell types and assessing whether two adjacent cells are interacting. Herein, our objective was to design an automatic procedure which would take as input 3D stacks of images of CTLs interacting with target cells to identify the CTL/target cell conjugates.

To achieve this, cells were stained with DAPI (*cyan*, to detect CTL and target cell nuclei), with antibodies directed against α -tubulin (*green*, to visualize the cytoskeleton in both cells), and perforin (*magenta*, a lytic molecule expressed only by CTLs) to allow Kartezio to distinguish the CTLs from the targets (**Fig. 5a**); individual channels from a representative image are displayed in **Extended Data Figure 2d**.

As previously illustrated in **Fig. 4b**, Kartezio-generated pipelines were sequentially applied to each layer of the z-stack. This process generated paired images of masks and markers (**Fig. 5b**). All the obtained pairs were then merged using an averaging function (see **Materials and Methods**) to produce one mask heatmap and one marker heatmap (**Fig. 5c**). Watershed was then applied to the heatmaps to produce 2D masks containing distinct segments of cells (**Fig. 5d**). At this step, Kartezio achieved an average AP50 score of 0.75 ± 0.025 over 35 runs during training with a maximum score of 0.81, and an average score of $0.67 (\pm 0.037)$ during testing on a validation set containing 150 previously unseen cells. These results are summarized in **Extended Data Table 5**. The best overall pipeline had a training score of 0.79 and a testing score of 0.72, and was utilized for the subsequent post-segmentation analysis.

At this stage of the image analysis, the segmented instances generated by Kartezio (each corresponding to exactly one cell, either CTL or target cell) were further analyzed using conventional image analysis approaches. Knowing the average dimensions of CTLs and target cells, we excluded all entities with a surface < 350 pixels ($\sim 24 \mu\text{m}^2$) and > 6000 pixel ($\sim 417 \mu\text{m}^2$), which might correspond to cell fragments or big cellular clusters. Additionally, we also applied a morphological closing to smooth cell contours. The next step, depicted in **Fig. 5e**, was to classify each instance as either CTL or target cell. To this end, we calculated the area and the intensity of DAPI (*cyan*), α -tubulin (*green*) and perforin

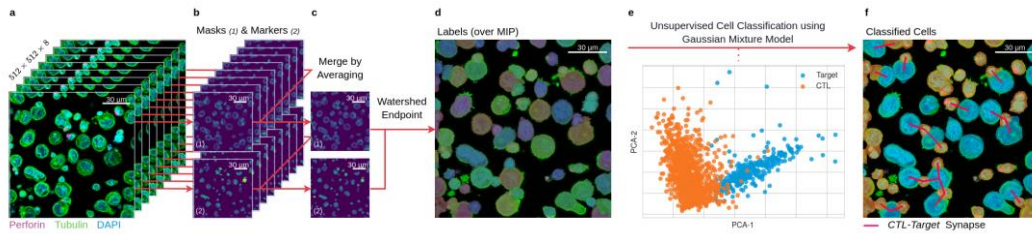


Fig. 5 |: A hybrid Kartezio/AI approach to detect CTL/target cell conjugates

Use Case 3: **a)** A mixed population of interacting cells containing both human clonal CTLs and target cells was stained with DAPI (cyan) and antibodies directed against α -tubulin (green) and perforin (magenta), as shown in **Extended Data Fig. 2d**. Each series of z-sections was used as a 3D input. **b)** The same Kartezio-generated instance segmentation pipeline was applied to each z-section to generate pairs of masks and markers. **c)** All masks and markers were merged to obtain one 2D mask heatmap and one 2D marker heatmap. **d)** The Watershed Endpoint was applied to generate 2D labels. **e)** During post-segmentation analysis, unsupervised Machine Learning (Principal Component Analysis followed by Gaussian Mixture Model) was used to classify the two-cell population. **f)** Visualization of cell classification. Colored masks indicate the two classes of cells, CTLs (orange) and target cells (blue). Red lines indicate putative synapses between CTLs and target cells.

(magenta) fluorescence for each instance. We considered these four features sufficient to separate the two cell populations since CTLs are statistically smaller than target cells and express perforin. Unsupervised machine learning using Principal Component Analysis (PCA) [32, 33] followed by Gaussian Mixture Model (GMM, see **Material and Methods**) was then used to separate the two population of cells. This method allowed us to reach an accuracy of 92.2 % on a validation set containing 153 cells, as evaluated against the ground truth established by independent analyzers.

Once the CTL and target cells were identified, we selected CTL/target cell conjugates based on their contiguity using the following two complementary procedures: i) we calculated the distance between the centroid of the CTL and the target cell masks and kept only the cells with a distance less than 70 pixels ($\sim 18.5 \mu\text{m}$). This procedure allowed us to keep in the analysis CTL and target cells with high probability of contact; and ii) in the selected conjugates, each target cell mask was slightly dilated to potentially intersect with other masks. This procedure was required since IS produces distinct (i.e. non-overlapping) masks. If an intersection with a CTL mask was detected, the target cell was considered in conjugation with the T cell (**Fig. 5f**).

Cumulatively, our procedure allowed us to keep in the analysis *bona fide* conjugates while excluding big cellular clusters and cell fragments. Each conjugate included in the analysis was verified by independent analyzers, showing an accuracy of the combined procedure of 75,4% on 52 lytic synapses.

In conclusion, the above results highlight a two-step approach, in which Kartezio can identify cells that are then classified by ML into different cell populations on the basis of their size and staining features. This offers the opportunity to explore automatic high-throughput scoring of defined parameters of immunological synapse formation and of other cell activation/death parameters in cell-cell conjugates. We show that Kartezio can synergize with state-of-the-art ML methods to create a hybrid AI approach capable of assessing and interpreting complex functional structures in biological images.

Use Case 4 - Tissue scale: segmenting tumor nodules in immunohistochemistry-stained tissue samples

We next proposed an end-to-end translational application of Kartezio for tumor nodule SS in patient tissue samples. The goal was to provide clinicians with an easy-to-apply and fully interpretable tool that is automatically generated starting from a small annotated dataset. These images are at both a higher scale and lower resolution than the previous Use Cases. For an initial application, we profited from two off-the-shelf tissue sample cohorts of metastatic melanoma patients we have previously described [34]. In this application, Kartezio was employed to create a SS mask of tumor nodules within IHC-stained tissue samples. Melanoma cells and T cells were identified by Sox10 (a nuclear marker of melanocytic lineage, *orange*) and CD8 (a CTL marker, *purple*) expression respectively and cell lysosomal content was identified by CD107a staining (*black*). All cells were counterstained with hematoxylin (*blue*).

In the present study, images were preprocessed by transforming R-G-B channels into H-S-V color space (**Extended Data Fig. 2e**). We limited the analysis to a dataset containing 24 images. **Fig. 6a** (*upper images*) depicts the 12 images used for training; **Fig. 6b** (*upper images*) depicts the remaining 12 images used for testing. Both image series have been annotated by an expert pathologist (*green lines*). Based on 100 runs, Kartezio obtained a mean IoU score of 0.84 (± 0.038) on the training dataset, with a maximum score of 0.89, as shown in **Extended Data Table 5**. Kartezio obtained a mean score of 0.82 (± 0.062) on the test dataset, with a maximum score of 0.89.

As shown in **Fig. 6a-b** (*lower images*), we merged the predictions of 100 trained models to generate heatmaps providing integrated representations of the obtained masks. To reach a consensus in line with expert pathologist annotation, only pixels with 75% of virtual experts agreeing on tumor area identification were displayed. In clinical settings, this threshold can be fine-tuned on the basis of the image cohort specificities and the expert pathologist's judgement.

Notably, each Kartezio-generated algorithm could be interpreted and explained. As an example, we selected the pipeline that obtained the best IoU score and dissected its behavior (**Fig. 6c**). The first step (node 3) of this pipeline consisted of subtracting the Hue channel (node 0) from the Saturation channel (node 1), allowing for the exclusion of pixels corresponding to CD8⁺ T cells and to other cells belonging to the tumor microenvironment. Then Kartezio used a Gaussian Blur filter (node 4) in order to smooth the previously obtained area. Next, Kartezio chose a Laplacian filter (node 10) to detect the variations in the image obtained in node 4, thus delimiting the tumor borders. Interestingly, the sequence Gaussian Blur/Laplacian filters is frequently used by image analysts for image segmentation tasks. To highlight the segmented areas, Kartezio used Morphological Black Hat (node 17) which reveals small objects that are darker than their surroundings. Altogether, these initial calculations provided an accurate estimation of tumor area.

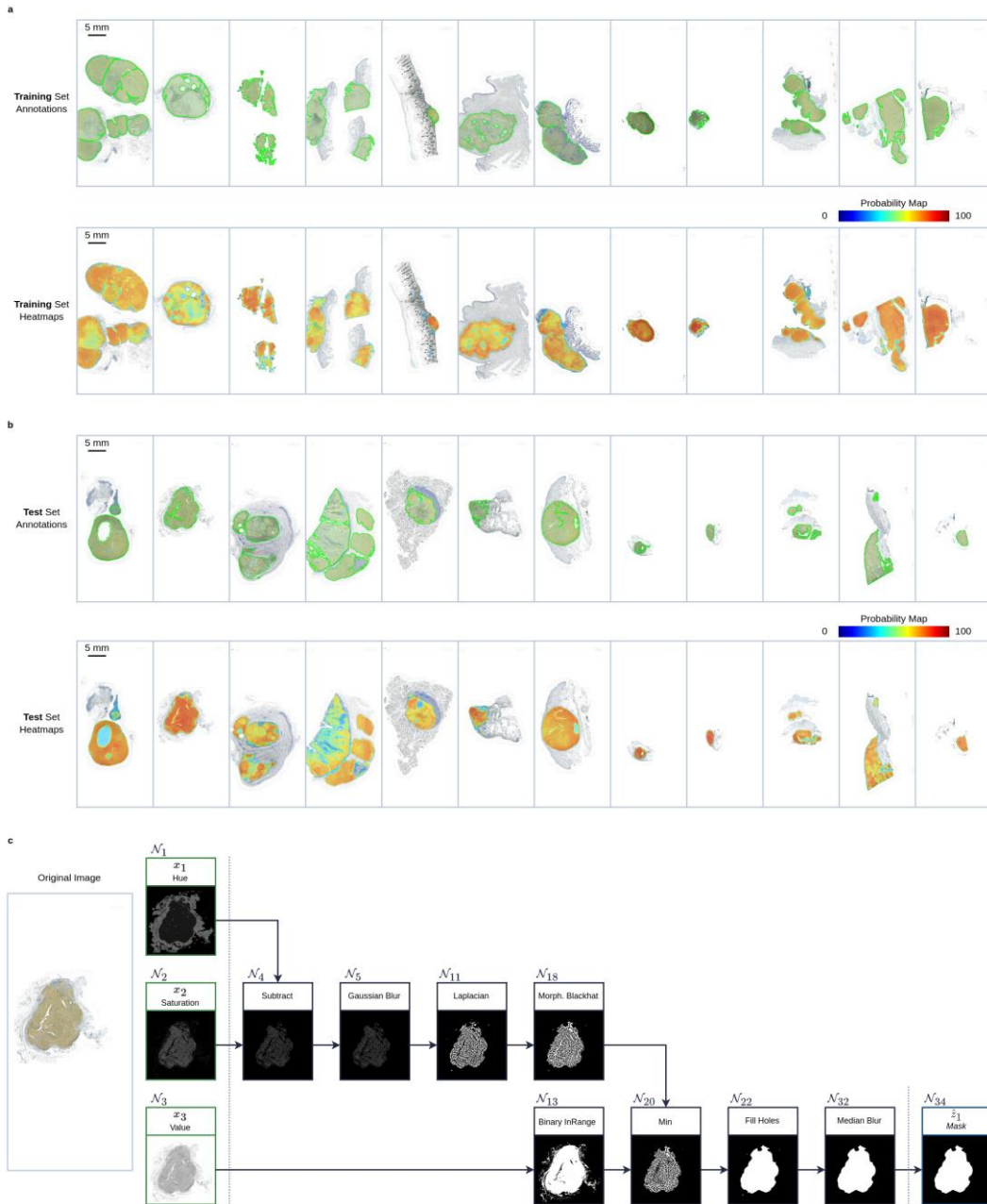


Fig. 6 | Segmentation of tumor nodules within IHC-stained tissue specimens

Use Case 4: a,b) Tumor nodule datasets comprised of fixed tissue slices stained for Sox10 (orange), CD8 (purple), CD107a (black) and counterstained with hematoxylin (blue) were used for training (a) and testing (b) of a Kartezio-generated semantic segmentation pipeline. Upper panels depict tumor contours as delineated by an expert pathologist (green lines). Lower panels depict the predictions of 100 Kartezio-generated models that have been merged to generate mask heatmaps of tumor contours. c) The pipeline that obtained the best IoU score is shown.

In parallel, node 12 created a binary mask of the Value channel (brightness) allowing for the establishment of a global map of the area of interest. The next step selected by Kartezio consisted of merging the two maps with the min operator (node 19). This allowed for the elimination of all pixels detected by the first calculation (results of node 17) that fell outside the area of interest. Kartezio next selected a Fill Hole filter in order to transform the selected area limits into a solid binary mask. A final step consisted of removing the noise from the edges of the mask using a Median Blur filter (node 31). In its entirety, the described process

allowed for the sharp delimitation of tumor nodules with a high degree of accuracy. Crucially, a step-by-step dissection of Kartezio's pipeline, similar to the one we outlined above as an example, can be applied to each pipeline.

This easily interpretable tool to rapidly segment tumor nodules has the potential to allow automatic assessment of various parameters that are critical for cancer patient management, such as tumor nodule size, morphological features, tumor localization, its borders with surrounding tissue, and distance from the resection margins, as described in more detail in the discussion below.

Discussion

In the present study, we release an innovative new computational tool called Kartezio for image segmentation of biological and medical images that draws inspiration from Darwinian evolution to automatically generate image processing pipelines. When compared head-to-head with DL approaches, Kartezio consistently achieved scores that were competitive with state-of-the-art approaches (**Fig.2, Extended Data Table 2**), despite being trained on only a very limited number of input images. We applied our approach to four distinct Use Cases (**Fig. 3-6**, summarized in **Extended Data Table 3**) related to tumor immunotherapy, a highly dynamic research area in contemporary medicine wherein automated image analysis has garnered significant interest[35, 36]. We validated Kartezio on tasks ranging from the characterization of nanometer-scale extracellular vesicles released by CTLs (average mask diameter of $\sim 0.6\mu\text{m}$, based on manual user annotations) to micrometer-scale analysis of CTL phenotype (average mask diameter of $\sim 12\mu\text{m}$, based on manual user annotations), and ultimately to centimeter-scale detection of cancer nodules in patient tissue samples (average estimated mask diameter of $\sim 1.1\text{cm}$, based on pathologist annotations). This stringent testing strategy provided a crucial validation of Kartezio's capabilities across a wide variety of image types and across scales differing by five orders of magnitude.

A conceptual step-by-step summary of the Kartezio workflow is illustrated in **Extended Data Fig. 1**. The experimentalist first prepares the training and testing datasets by manually annotating a limited number of images. Then, the training images are provided to Kartezio, which generates initial pipelines composed of functions randomly drawn from the default function library, randomly parameterized and randomly arranged into an image processing pipeline. Each pipeline is evaluated against user defined annotations and the best pipeline is selected to proceed through the evolutionary selection process (illustrated in **Extended Data Movie 1**). The optimized pipeline proceeds to the testing phase and, if satisfactory, it can be then deployed on a previously unseen dataset.

As demonstrated in the four Use Cases, once image segmentation (IS or SS) has been achieved using Kartezio, post-segmentation analysis of the segmented images can be performed, ranging from simple feature extraction from instances (e.g. MFI, size of particle, etc.) to ML-based analyses, depending upon the experimental design and needs of the experimentalist (illustrated for the four Use Cases in **Extended Data Table 3**).

Our work tackles two major scientific challenges in the fields of CV and biomedicine. Firstly, it is becoming increasingly important to generate fully explicable image analysis strategies and to track the logic of decisions made by algorithms to ensure responsible patient management. Unlike Kartezio, the so-called "black box" DNN networks are difficult for humans to analyze and interpret, in spite of recent progress in the field of XAI [5, 6]. Limited interpretability is a potentially important drawback, particularly in the clinical context, where the process of extracting information from medical images should be fully transparent and interpretable in order to foster trust, ensure compliance with professional ethical standards, and facilitate regulatory oversight. This is also in line with the main principles of the European Union AI Act[37], currently under discussion by the European Council, that regulates the use of AI in sensitive fields such transportation and health care. As shown in **Fig. 6**, Kartezio is natively interpretable, meaning that the generated pipelines can be humanly read, evaluated and tested for provability. Given the

potential applications for Kartezio in clinical pathology and related fields, its fully interpretable “white-box” nature presents a major conceptual advantage[13].

Secondly, image annotation is a time-consuming task that requires high biomedical expertise. It is therefore crucial to minimize experts' effort by designing ML algorithms that can handle the smallest datasets possible, while keeping adequate generalization capacity. To address this point, our study utilizes CGP to generate solutions that leverage the cumulative expertise of human CV experts. In other words, CGP produces pipelines by assembling algorithms that integrate decades of existing research and development in CV. While the number of images used in our study is already remarkably low, it is conceivable to upgrade Kartezio to an active “human-in-the-loop” training mode to further reduce the size requirement of the training dataset and improve performance. In such a configuration, intermediate results from Kartezio-generated pipelines could be displayed while the expert annotates. At a given point, the expert would not annotate anymore, but simply amend the automatically generated annotation. In turn, expert-operated adjustments would be informative to pursue the training of Kartezio.

In addition to these major conceptual advantages, Kartezio offers several concrete technical improvements over existing IS approaches. For example, Kartezio can handle images of diverse size within the same dataset. In addition, it can be trained on small patches and later deployed on much larger images. Finally, Kartezio is not restricted to gray scale input images and can easily accommodate RGB, HSV (Hue Saturation Value), and HED (Hematoxylin Eosin Diaminobenzidine) formats.

Nonetheless, there are certain limitations to bear in mind when assessing the applications of Kartezio. For example, while the pipeline shown in **Fig. 6** is clear, streamlined and explicable, there is no guarantee that all Kartezio-generated pipelines will be so intuitive to understand. This is particularly salient if the predetermined number of nodes is high and/or the number of available functions in the function library is high. In the field of evolutionary computation, research is ongoing to take into account the size of the graph in the evaluation process using multi-objective optimization[38-40]. Another complementary approach to control graph size can come from automatic modularization strategies of produced graphs[41]. Further research is required to explore and apply these solutions to Kartezio.

An additional caveat when using CGP-mediated analysis concerns the configuration of the function library. Specific expertise is necessary to find the minimal set of functions that can solve adequately the task while keeping the dimensions of the search space as small as possible. The current version of Kartezio contains 42 functions that have been manually selected to address the specific tasks of this study. A possible improvement of Kartezio would be to automatically select functions included in existing programming libraries to generate *ad hoc* CGP libraries suitable for a given task. In this case study, Kartezio was applied to the task of IS, but this approach could clearly be applied to other tasks in the CV field as long as pre-existing functions are available and already used by human-made algorithms.

It is important to note that in the present configuration, Kartezio only handles images. However, in biomedicine a plethora of data is collected in different formats and must be analyzed in an integrated fashion. In biology, these data may be derived from diverse

molecular and functional experiments, as well as from microscopy. In medical practice, these clinical data may include laboratory test results, demographic, lifestyle and prognostic factors, and imaging data from diverse sources (e.g. histopathology, PET scans, etc). Mixed-Type CGP (**MT-CGP**) [42] is a promising approach to handle and integrate heterogenous data, such as scalars, vectors and matrices. Upgrading Kartezio in this direction would allow us to create data analysis pipelines that, while remaining fully explainable, would integrate data of different kind and origin. In clinical routine, such an approach would endow practitioners with AI-based clinical assistants that would be compatible with the upcoming regulatory guidelines.

In biological research, only a fraction of generated data is included in publications. Experimental data are indeed often analyzed only to answer specific questions, but are rarely used for broader integrated analyses. Such deep analyses are time and energy consuming and might not provide results immediately beneficial to the advancement of a given research. They may therefore be neglected. Kartezio could be trained at low human cost on small datasets to automatically extract predefined features (geometrical information from images, intensity of staining from flow cytometry data, activation of death pathways in target cells, single cell mRNAseq data, etc). These extracted data would feed large pre-analyzed data bases that could be used by data scientists to address new questions using mathematical and ML approaches.

An additional important benefit of Kartezio's application to microscopy concerns the necessity of limiting the subjectivity of the experimentalists who analyze and scores the images. A way to bypass the problem of subjective image scoring is the use of high-throughput techniques such as high-content imaging and imaging flow cytometry (e.g. ImageStream™) that permit the rapid acquisition of thousands of biological images and subsequent analysis of these images using dedicated bulk software[43]. While these high-throughput imaging techniques are very powerful and are useful under many circumstances, they lack resolution. As a consequence, their utility is limited to the analysis of bulk cellular/subcellular structures. The application of Kartezio to high-resolution, super-resolution, and even electron microscopy images can in principle ensure automated non-subjective analysis with no compromise in terms of resolution.

The ability to reconcile automated image analysis with high-resolution imaging is particularly important in the field of nanomedicine, wherein nanotechnologies are applied to diagnostics, therapeutics, vaccines etc. Indeed, characterization of drug vectors and bioactive particles requires the implementation of methods that allow researchers to effectively evaluate and optimize parameters such as particle size and composition. In this sense, Kartezio offers a first stepping stone to address this issue by rapidly creating pipelines for analysis of subcellular structures, such as CTL-derived extracellular particles (**Fig. 3**). Further optimization of Kartezio is required to make it a reliable "pharmacologist assistant" for validation of nanometer/micrometer size therapeutical preparations.

In summary, Kartezio offers a robust, flexible, and ground-breaking approach to automated image processing. It facilitates the generation of specialist models starting from small or very small datasets. This confers upon Kartezio an exceptional level of versatility and broadens its potential applications to include contexts in which large datasets are unavailable or unattainable. Although in our study we applied Kartezio to biomedical

images, its application can be extended to different fields. It is interesting to note that one of the first application of CGP to image analysis comes from a study in which CGP was applied to images acquired by a Mars rover [11]. Taken together, our study and these pioneering observations strongly suggest that CGP will become increasingly important in the development of CV and in its application to different aspects of human life.

Material and Methods

Mathematical modelling

Kartezio was developed using Python3[44] programming language and built mainly over NumPy[45], OpenCV[46], Scikit-image[47], and Scikit-learn[33]. For the visualization, images and plots were generated using Matplotlib[48], Seaborn[49], OpenCV[46], and Fiji[50].

Kartezio Parameters

Symbol	Description
$\iota \in \mathbb{N}_{\geq 1}$	Number of inputs for the CGP model; also the size of X
$\eta \in \mathbb{N}_{\geq 1}$	Number of nodes for the CGP model
$o \in \mathbb{N}_{\geq 1}$	Number of outputs for the CGP model; also the size of \hat{Z}
$\alpha \in \mathbb{N}_{\geq 1}$	Global arity for all the functions of the library
$\rho \in \mathbb{N}_{\geq 0}$	Global number of parameters for all the functions
$\lambda \in \mathbb{N}_{\geq 1}$	Number of children of the population involved in Evolution Strategy $1 + \lambda$
μ	Mutation probability for functional nodes
ν	Mutation probability for output addresses
$\mathcal{K} \in \mathbb{N}_{\geq 1}$	Number of iterations for the evolution loop

Kartezio Data

Symbol	Description
$X: \{x_1 \cdots x_\iota\}$	Formatted input vector of ι elements
$\hat{Z}: \{\hat{z}_1 \cdots \hat{z}_o\}$	Intermediate output vector of o elements
\hat{Y}	Finale output produced by the Endpoint \mathcal{E}
Y	Ground truth annotations
\mathcal{X}_{set}	Training or test set; list of many X inputs
\mathcal{Y}_{set}	Training or test set annotations; list of many Y

Kartezio Model Components

Symbol	Description
\mathcal{G}	Genotype (genome, individual, chromosome)
\mathcal{P}	Phenotype (syntactic graph, pipeline)
\mathcal{N}	Node
\mathcal{E}	Endpoint
$L: \{f_1 \cdots f_\varphi\}$	Function library composed of φ functions f
\mathcal{F}	Fitness minimization function

Kartezio Operators

Symbol	Description
$\delta: \mathcal{G} \rightarrow \mathcal{P}$	Decodes to parse one Genotype to the active Phenotype
ψ	Executes the Phenotype function sequence
ε	Executes the Endpoint to produce the final output \hat{Y}

Cartesian Genetic Programming

Genome. CGP considers a specific encoding of the syntactic graph within integer-based genome (**Fig. 1a**). Each node \mathcal{N}_i (encoded in a gene) of the graph is identified with the unique integer value i that the other graph nodes will address to connect the mathematical functions. Here, the genome \mathcal{G} of a CGP oriented graph \mathcal{P} is an m -by- n matrix where m is the number of nodes and is equal to the total number of functional nodes (η) and output nodes (o). n corresponds to the size of one node, which relies on 3 values: the unique function index from the function library L , the number of inputs for the functions (α), which correspond to the maximal arity of the functions from the library and the maximum number of parameters (ρ) required by the functions from the library. Formally, the genome can be written as 2 sub-matrices:

$$\mathcal{G} = \begin{bmatrix} \mathcal{N}_{\eta \times n} \\ \mathcal{O}_{o \times n} \end{bmatrix} \in \mathcal{M}_{m \times n}(\mathbb{N}) \quad \text{where} \quad \begin{aligned} m &= \eta + o \\ n &= 1 + \alpha + \rho \end{aligned}$$

Nodes. A functional node \mathcal{N}_i is a 1-D vector composed of 3 significant segments described as follows:

$$\mathcal{N}_i \in \mathcal{M}_{1 \times n}(\mathbb{N}): [b_i, C_i, P_i] \quad \text{where} \quad \begin{aligned} b_i &\in [1, \varphi] \\ \forall c \in C_i, c &< i \end{aligned}$$

where the integer b_i indexes one of mathematical functions from L (**Extended Data Table 1**), C_i are addresses of upstream nodes within the graph that will be used as inputs of the node's function and P_i are constant (but optimized) parameters of the function. All functions from the library must be determinist and must return one 2D image which is identical to the input image in dimensions and type (generally encoded in uint8). Most of the time, one node operation consists of one function call from the OpenCV Python package. All functions must be image-size independent, which implies that the input and output for a given image is equivalent. However, there is no image size constraint for the model in both training and test datasets.

The first ι nodes, noted as $X: \{x_1 \cdots x_\iota\}$ are the receiving inputs (e.g. image channels) while the last o nodes represents the intermediate outputs $\hat{Z}: \{\hat{z}_1 \cdots \hat{z}_o\}$.

An example of genome $\mathcal{G}[\iota = 3, \eta = 6, o = 2, \alpha = 2, \rho = 1]$ with its nodes is illustrated in **Fig.1**.

Non-evolvable Preprocessing Node. The first stage of a standard image processing pipeline is the preprocessing or/and formatting of the raw data. Depending on the input images (e.g. transmission light images, fluorescent images, IHC tissues images, etc.) and the expected outcomes (e.g. cell identification, event counting, cell distance and interaction, etc.) needed to address a given biological question, the user can impose a preprocessing of the dataset. When loading the dataset, the preprocessing stage is done on-the-fly and produces a formatted input X for each entry of the dataset. For example, the default behavior for a standard bitmap image is $X_{rgb}: [x_1 = r, x_2 = g, x_3 = b]$. For specific needs of certain datasets, any function can be used for preprocessing (e.g. HSV transformation, pyramidal mean shift filtering, etc.) including those requiring all three

channels to operate. This can help evolution by providing important insight given by the domain expert.

Non-evolvable Endpoint. We also introduce a new component extending CGP to IS using a determined final function called Endpoint. It is the last processing step before evaluation. It is a substantial bottleneck, not subject to optimization, of the syntactic graph. Moreover, the endpoint is the only node allowing the outcome size and type to change. We use Watershed Transform as the main algorithm to produce IS. In cell segmentation, the cell nuclei are usually stained or visible, so it is possible to deduce good markers for a Marker-Controlled Watershed ($\sigma = 2$). These two endpoints produce a label map that is then assessed. After evolution, the genome endpoint can be enhanced with deployment features like ImageJ ROI generation based on labels. In SS, the default endpoint is a Threshold (*binary or to zero*).

Genome Decoding and Graph Execution. To generate an output from given inputs, the CGP genome \mathcal{G} is first decoded to produce its phenotype \mathcal{P} (**Equation 1**). \mathcal{P} is then executed to produce the intermediary results $\hat{\mathcal{Z}}_{\mathcal{G},X}$ (**Equation 2**) which is provided as the input of the endpoint (**Equation 3**) to calculate the final output $\hat{\mathcal{Y}}_{\mathcal{G},X}$.

$$\mathcal{P} = \delta(\mathcal{G}) \quad (1)$$

$$\hat{\mathcal{Z}}_{\mathcal{G},X} = \psi(\mathcal{P}, X) \quad (2)$$

$$\hat{\mathcal{Y}}_{\mathcal{G},X} = \varepsilon(\hat{\mathcal{Z}}_{\mathcal{G},X}) \quad (3)$$

When used on 3D images, Equation 1 is used only once to obtain a unique syntactic graph which will be used for all z-sections. Equation 2 is executed for each z-section X_z of the image. All $\hat{\mathcal{Z}}_{\mathcal{G},X_z}$ are then merged (averaged in the example **Equation 4**) to obtain the intermediary output $\hat{\mathcal{Z}}_{\mathcal{G},X}$, which is in turn feeding the endpoint (**Equation 3**) to produce the final output $\hat{\mathcal{Y}}_{\mathcal{G},X}$.

$$\hat{\mathcal{Y}}_{\mathcal{G},X} = \varepsilon\left(\frac{1}{N} \times \sum_{z=1}^N \hat{\mathcal{Z}}_{\mathcal{G},X_z}\right) \quad (4)$$

Evolution. Kartezio uses the $1 + \lambda$ Evolution Strategy (**ES**). A first population ($k = 0$) of genomes $\mathcal{G}_{k=0}^n$ with $n \in [0, \lambda]$ is initialized randomly and independently. These genomes then follow an evolutionary loop in which they will first be evaluated and the best genome $\mathcal{G}_{k=0}^*$ selected based on evaluation score to produce the next parent genome. $\mathcal{G}_{k=1}^*$ is then mutated to produce λ offspring $\mathcal{G}_{k=1}^n$ with $n \in [1, \lambda]$. The evolutionary loop (evaluation, selection, mutation) is repeated a finite number of \mathcal{K} iterations to produce the final genome $\mathcal{G}_{\mathcal{K}}^*$. The following section details each evolutionary operator, the $1 + \lambda$ ES.

Evaluation. To evaluate a genome \mathcal{G} , this genome is first decoded as describe previously. The resulting graph is executed on each image of the training dataset \mathcal{X}_{train} to obtain a set of predictions $\hat{\mathcal{Y}}_{\mathcal{X}}$. Predictions are confronted to the ground truth of the dataset \mathcal{Y}_{train} using

a specific fitness function \mathcal{F} which evaluates the prediction errors. This function is domain-specific (e.g. AP50 for IS or IoU for SS) and must be defined for each task Kartezio is used for. The genome evaluation is finally given by the average of prediction error:

$$fitness_g = \frac{1}{N} \times \sum_{i=1}^N \mathcal{F}(y_{train_i}, \hat{y}_{x_i})$$

Selection. The objective is to minimize the prediction error over many iterations. The best genome is therefore selected among the offspring and the parent by selecting the smallest prediction error. If an offspring obtains a fitness strictly equal to the current parent, they are distinguished by minimizing the execution time of the graph to promote frugality in term of computational effort.

Mutation. The parent generates λ new offspring by mutation. Mutations consist of randomly altering random values of the genome. Kartezio performs mutations until the active graph changes (Accumulate) as described in [51]. Random indices (i, j) are sampled in the whole functional submatrix: $\mathcal{G}_{i,j}$ gets a new independent value r , sampled as follows:

$$\mathcal{G}_{i,j} = \begin{cases} r \in [1, \varphi] & \text{if } j = 1 \\ r \in [1, i[& \text{if } 1 < j < 1 + \alpha \\ r \in [0, 255] & \text{if } 1 + \alpha < j < 1 + \alpha + \rho \end{cases}$$

The number of altered $\mathcal{G}_{i,j}$ values (respecting point mutation) is calculated to respect the mutation rate parameter. Lastly, each output address has a probability to be replaced by a new random value $r \in [1, \iota + \eta]$.

Benchmarking. We trained the models with a $\eta = 30$ nodes, $\lambda = 5$ offspring over $\mathcal{K} = 20,000$ iterations. If the parent reached a score of 0, the evolution process stopped as no prediction error was made on the training dataset. The mutation probability was $\mu = 0.15$ for the functional nodes and $\nu = 0.2$ for the outputs. 35 independent runs were made for each experiment for statistical purposes. They were run on a bi Intel Xeon @6140 (2×18 cores, 2.30GHz - 3.70GHz) with 192Go of memory.

Applications of Kartezio

Standardized Testing Using Published Cell Image Library (Fig. 2, Extended Data Fig. 2a)

We compared Kartezio to three state-of-the-art IS algorithms: Cellpose, StarDist and Mask R-CNN. To this end, the dataset and the results for these three algorithms were taken from published data [21]. The dataset was composed of 100 images of *in vitro* cultured neurons stained for phalloidin and DAPI (as shown in **Extended Data Fig. 2a**) and imaged using an epifluorescence microscope. The dataset was split into 89 images for training and 11 images for testing. No data augmentation was necessary for our approach.

In this study case, Kartezio was composed of $\iota = 2$ inputs, corresponding to the α -tubulin and DAPI channels, and $o = 2$ outputs, corresponding to the mask and markers necessary for the Watershed Transform non-evolvable endpoint. Generated syntactic graphs were evaluated using the Average Precision ($AP = \frac{TP}{TP+FP+FN}$) metric calculated with the

standard IoU between the predicted mask and the ground truth. A threshold of $t = 0.5$ was applied to decide the correctness (true-positive) of the predicted mask, as described[21]. Kartezio was benchmarked on different training dataset sizes, ranging from 1 image to 89 images. For each size of dataset, images were randomly selected from the initial 89 training images. Each trained solution was evaluated with the same 11 test images. Experiments were repeated 35 independent times for statistical purposes. Following this, we assembled four Use Cases with different model inputs and outputs (summarized in **Extended Table 4**) to illustrate Kartezio's versatility.

Use Case 1 - Extracellular Particles (Fig. 3, Extended Data Fig. 2b)

Because of the intensity difference between channels (shown in **Extended Data Fig. 2b**), the dataset was split into two datasets, one to generate a WGA specialist model and one to generate a DiO specialist model. The same procedure was applied to both WGA and DiO datasets. Each dataset included one training image and one testing image of CTL-derived extracellular particles. Training and testing sets were augmented by splitting each image into four quarters. The final post-segmentation analysis was made using the test and training images combined with nine previously unseen images. Use Case 1 dataset preparation is summarized in **Extended Data Table 3**.

As shown in **Extended Data Table 4**, Kartezio used $\iota = 1$ channel either for WGA or for DiO and $o = 1$ outputs that produces mask. This mask was passed to the Local-Max Watershed non-evolvable endpoint, which consisted of creating a Distance-Transform (DT) map from the mask to find local-max (peaks). Together the peaks and the smoothed gradients of the DT were provided as input to Watershed Transform. Generated syntactic graphs were evaluated as described in the first study case.

Once trained, both models generated masks containing prediction of WGA particle and DiO particle instances. The two masks were merged using the same procedure to evaluate mask prediction to expected ground truth (IoU with a threshold of 0.05).

Use Case 2 – CTL Lytic Arsenal (Fig .4, Extended Data Fig. 2c)

From the original set of 19 images, 5 images were selected for the training dataset and 4 for the test dataset. Each 3D image was composed of 4 channels. Use Case 2 dataset preparation is summarized in **Extended Data Table 3**. To reduce the computational cost, we resized the images (halved the size). We chose a threshold $t = 0.7$ for the fitness function (AP70) to be more stringent with the predicted mask. To process a 3D image, we provided the z-sections of $\iota = 1$ channel (CD45) to the model, which generates $o = 1$ mask (as summarized in **Extended Data Table 4**). All the masks were averaged to produce one final mask of the whole 3D image. We then applied the Local-Max Watershed Endpoint to produce the final 2D IS. Cells were segmented from the 19 original images using the best model out of 35 runs. 161 cells were filtered from predicted cells using their pixel area ($2000\text{px} < \text{area} < 14000\text{px}$). For each cell, we calculated intensity features (see below) based on the perforin, granzyme B and CD107a channels (shown in **Extended Data Fig. 2c**). All the cell's feature vectors were then used to generate the UMAPs [31] of **Fig. 4**. To this end, we used the following parameters to the UMAP function: dimensionality reduction down to 2 components, using following parameters: n_neighbors=15, min_dist=0.01.

Use Case 3 - Lytic Synapses (Fig. 5, Extended Data Fig. 2d)

Four 3D images (using the z-stack function) were acquired. These large images were cut into a 3x3 grid, with a depth interval set for each tile (adapted to the focus). Images with high background noise and culture well edges were removed, thus giving a total of 32 selected images (representative image shown in **Extended Data Fig. 2d**). We randomly extracted 8 images for the training set and 4 for the test set (summarized in **Extended Data Table 3**). As shown in **Extended Data Table 4**, the models handled $\iota = 2$ channels (α -tubulin, DAPI) and used the Watershed endpoint ($o = 2$). Similar to the previous application, each z-section produced one markers map and one mask map, which were averaged individually before being passed to the Endpoint. In that case, the models segmented cells with no distinction of types. Over the 32 images, predicted cells were filtered by pixel area ($350 < \text{area} < 6000$).

Segmented cells were then classified as either CTLs or target cells by using their intensity feature vector (see below) combined with their area. Unsupervised learning was used for classification using first Principal Component Analysis ($n_components = "mle"$) followed by a Gaussian Mixture Model (**GMM**) ($n_components = 2, covariance_type = "tied"$).

Finally, CTL/target cell synapses were detected when the Euclidian distance between the centroids of a CTL and a target cell was less than 70px (\sim nm). The target cell masks of potential synapses were then dilated (morphological dilation) to assess potential overlapping with CTL mask. A valid CTL/target cell synapse was detected if at least one pixel was overlapping.

Use Case 4 - Tumor Nodules (Fig. 6, Extended Data Fig. 2e)

A set of 24 whole-slide images from the clinical cohort was assembled for training and testing, including 12 images from each clinical site (Institut Universitaire du Cancer de Toulouse and Centre Hospitalier Universitaire de *Bordeaux*). Images were allocated in a randomized fashion into the training ($n = 12$) and testing ($n = 12$) sets (summarized in **Extended Data Table 3**). Whole-slide high-resolution images were first saved at their lowest resolution level, strongly reducing image size. Images were preprocessed by transforming R-G-B channels into H-S-V color space (shown in **Extended Data Fig. 2e**). As summarized in **Extended Data Table 4**, Kartezio's models were trained with $\iota = 3$ inputs and terminated with a Threshold to zeros endpoint ($o = 1$). Evaluation was made using the simple IoU Fitness function.

100 models were trained to segment tumor nodules. Each prediction from individual models was normalized (minmax scaler). All 100 predictions were merged by averaging the values pixelwise. All in all, the heat map \mathcal{H} of one slide X is obtained by:

$$\mathcal{H} = \frac{1}{N} \times \sum_{i=1}^N \frac{\hat{Y}_{g_i, X} - \min(\hat{Y}_{g_i, X})}{\max(\hat{Y}_{g_i, X}) - \min(\hat{Y}_{g_i, X})} \quad \text{where } N = 100$$

The heat maps were then thresholded *to zeros* ($t = 0.25$) to produce the heat maps presented in **Fig. 6a-b**.

Intensity Feature Vector. This vector contained individual and combined counts of positive pixels, the sum, and the average pixel fluorescence intensities. Combined counts were calculated by first applying a binary threshold to determine the positive pixels within each channel. Each pixel of a given cell mask incremented a counter corresponding to its combination of positive channels. All the counters, augmented with the total count, the sum and the average fluorescence intensity for each channel were gathered into the intensity feature vector. The length ℓ of the vector was determined by the number of channels \mathcal{C} :

$$\ell = 2^{\mathcal{C}} + 3 \times \mathcal{C}$$

Image acquisition and processing

Preparation of extracellular particles and single particle imaging

For preparation of extracellular particles (EPs), CD8⁺ human primary T cells were isolated from healthy donor blood with negative selection kits (RosetteSep Human CD8⁺ T cell Enrichment Cocktail, STEMCELL Technologies, UK) following the manufacturers instruction. Peripheral blood samples were provided from the National Health Service under ethics agreement number 11/H711/7. CD8⁺ cells were expanded after isolation by addition of anti-CD3/anti-CD28 T-cell activation beads (Dynabeads ThermoFisher Scientific, UK) at 25 μ l/ 10⁶ cells and with 5000 Units/ml recombinant IL-2 for 3 days following the manufacturer's instructions. Subsequently, the magnetic beads were removed and cells were rested for 4 days at 10⁶ cells/ml. For all incubation steps, cells were cultured in RPMI (Gibco) medium supplemented with 10% fetal bovine serum, 1% penicillin/streptomycin, 1% L-glutamine, 1% non-essential amino acids and 50 mM HEPES in cell culture treated flasks at 37°C, 5% CO₂ and 100% humidity.

After resting, cells were transferred to fully-supplemented culture medium containing exosome-depleted serum (Thermo Fischer Scientific, UK) and cultured for 48 hours. For EP isolation, the culture medium was subsequently collected (total of 50 ml) and cells were removed by centrifugation for 10 min at 300 g. Larger particles and cell debris were removed by centrifugation for 20 min at 900 g. Subsequently, EPs were collected by centrifugation for 60 min at 100,000 g and at 4°C. The EP pellet was resuspended in 1 ml phosphate buffered saline (PBS) and stored until further use at -20°C. Repeated thawing and freezing cycles were avoided.

The EP solution (total protein concentration of 137 μ g/ml) was diluted 1:10 with PBS and stained with a final concentration of 40 μ g/ml AlexaFluor647-coupled WGA (ThermoFisher Scientific, UK) and 20 μ M DiO (ThermoFisher Scientific, UK) for 1 hour at 4°C in the dark. 150 μ l of the EP sample were then deposited onto clean glass coverslip (SCHOTT UK Ltd, Stafford, UK) fixed to flow chambers (sticky- Slide VI 0.4, Ibidi, Thistle Scientific LTD, Glasgow, UK) that were coated with 0.1 mg/ml poly-L-lysine (Sigma Aldrich, UK) for 15 min and washed twice with PBS before addition of EPs. The EPs were incubated for 30 min at 4°C in the dark to allow for EP binding on the surface. Excess dye and non-bound EPs were washed from the flow channels by washing twice with PBS. Samples were subsequently imaged by TIRFM using an Olympus IX83 inverted microscope (Keymed, Southend-on-Sea, UK) equipped with 405-nm, 488-nm, 561-nm and

640-nm laser lines and a Photometrics Evolve delta EMCCD camera. Images were acquired with a 150x 1.45 NA oil-immersion objective.

Confocal microscopy

Staining for CTL lytic components.

Total CD8⁺ T cells were purified from healthy donor blood samples using the RosetteSep Human CD8⁺ T Cell Enrichment Cocktail (StemCell Technologies) following the manufacturers instruction. Blood samples were collected and processed following standard ethical procedures after obtaining written informed consent from each donor and approval by the French Ministry of the Research (transfer agreement AC-2020-3971). Approbation by the ethical department of the French Ministry of the Research for the preparation and conservation of cell lines and clones starting from healthy donor human blood samples has been obtained (authorization no. DC-2021-4673).

CD8⁺ T cells were cultured in RPMI 1640 medium supplemented with 5% human AB serum (Institut de Biotechnologies Jacques Boy), 50 μ M 2-mercaptoethanol, 10 mM Hepes, 1% MEM-Non-Essential Amino Acids (MEM-NEAA) Solution (Gibco), 1% sodium pyruvate (Sigma-Aldrich), ciprofloxacin (10 μ g/ml) (AppliChem), human recombinant interleukin-2 (rIL-2; 100 IU/ml), and human rIL-15 (50 ng/ml) (Miltenyi Biotec). CD8⁺ T cells were collected 7 days after activation using anti-CD3/anti-CD28 T-cell activation beads (Dynabeads ThermoFisher Scientific) at 2.5 μ l/ 10⁶ cells. Cells were washed in serum-free RPMI 1640 and allowed to adhere to poly-L-lysine (Sigma Aldrich) coated slides (Erie Scientific, ER-208B-CE24) at 37°C, 5% CO₂ for 10 min. Cells were then fixed with 3% paraformaldehyde (MP Biomedicals) for 10 min at room temperature, washed twice with PBS and subsequently permeabilized with 0.1% saponin (in PBS/3%BSA/HEPES). Cells were stained in a two-step process with primary antibodies followed by isotype matching secondary antibodies all at 10 μ g/ml. Both steps were performed for 1h at room temperature. We used the following antibodies: Anti-human perforin mAb (clone δ G9, IgG2b, BD 556434) followed by goat anti-mouse IgG2b AlexaFluor647 (Thermofisher A-21242), anti-human CD107a rabbit Ab (polyclonal, Abcam ab24170) followed by goat anti-rabbit AlexaFluor555 (Thermofisher A32732), anti-human granzyme B mAb (clone GB11, IgG1, Thermofisher MA1-80734) followed by goat anti-mouse IgG1 AlexaFluor488 (Thermofisher A-21121), and anti-human CD45 rat Ab (clone YAM1501.4, Thermofisher MA5-17687) followed by goat anti-rat AlexaFluor405 (Thermofisher A48261).

The samples were mounted in 90% glycerol-PBS containing 2.5% DABCO (Sigma). Randomly selected cells were imaged with a LSM 780 confocal microscope equipped with a 63x-NA 1.4 oil immersion Plan-Apochromat objective (Zeiss), zoom 1.0. Images were acquired as z-stacks with an interval of 0.75 μ m.

Staining for immunological synapse detection. Target cells were either unpulsed or pulsed with 10 μ M antigenic peptide for 2 h at 37 °C in RPMI 5% FCS/HEPES and washed three times. Conjugates were formed by 1 min centrifugation at 455g, incubated for 15 min, gently disrupted and seeded on Poly-L-Lysin coated slides and fixed with 3% paraformaldehyde at 37 °C. Cells were then permeabilized with 0.1% saponin (in PBS/3%BSA/HEPES), and stained with anti-human perforin mAb (10 μ g/ml, clone δ G9; BD Pharmingen) followed by AlexaFluor555 goat anti-mouse IgG2b (10 μ g/ml;

Invitrogen) and anti- α -tubulin mAb (1 μ g/ml, clone DMA1; Sigma) followed by AlexaFluor488 goat anti-mouse IgG1 (10 μ g/ml; Invitrogen). The samples were mounted in 90% glycerol-PBS containing 2.5% DABCO (Sigma) supplemented with DAPI (1 μ g/ml; Invitrogen) and examined using a LSM 780 (Zeiss) confocal microscope over a 63x Plan-Apochromat objective (1.4 oil). 3D images (using the tile scan and z-stack functions) were acquired.

Patient cohort

The established melanoma clinical cohort (previously described[34]) was comprised of patients treated for advanced melanoma both at the Oncodermatology Department of the Institut Universitaire du Cancer de Toulouse (IUCT) and at the Centre Hospitalier Universitaire (CHU) de Bordeaux. Samples in Toulouse were stored at the CRB Cancer des Hôpitaux de Toulouse collection. In accordance with French law, this cancer collection was declared to the Ministry of Higher Education and Research (DC-2020-4074) and a transfer agreement was obtained (AC-2020-4031) after approbation by ethical committees. Samples in Bordeaux were stored at the Cancer Biobank of CHU Bordeaux collection. In accordance with French law, this cancer collection was declared to the Ministry of Higher Education and Research (DC 2014-2164) and a transfer agreement was obtained (AC-2019-3595) after approbation by ethical committees. Patients with available formalin-fixed, paraffin-embedded (**FFPE**) tumor blocks at the Department of Pathology were included in the analysis.

Immunohistochemistry

As previously described[34], CD8, CD107a and Sox10 were visualized by multiplex immunohistochemistry for the entire tumor nodule and surrounding tissue. The Discovery ULTRA (Ventana Medical Systems, Innovation Park Drive Tucson, Arizona 85755 USA, ROCHE) was used for automated staining. After dewaxing, tissue slides were heat pre-treated using CC1 buffer (05424569001, ROCHE). Slides were stained using the RUO Discovery Universal procedure (v0.00.0370) in a 3 step protocol with sequential denaturation (CC2 buffer (pH6), at 100°C, 05279798001, ROCHE). Tissue slides were incubated using primary antibodies CD107a (clone D2D11, #9091, Cell Signaling Technology, Inc.), CD8 (clone C8/144B, M7103, Agilent Technologies) and Sox10 (clone SP267, 07560389001, ROCHE) in Envision Flex diluent (K800621-2 Agilent Technologies). Targets were then linked using the OmniMap anti-rabbit (05269679001, ROCHE) and OmniMap anti-mouse (05269652001, ROCHE) HRP conjugated secondary antibodies. Visualization of the different targets was performed using Discovery Silver (07053649001, ROCHE), Purple (07053983001, ROCHE) and Yellow (07698445001, ROCHE) detection kits. Tissue slides were counterstained using Haematoxylin (05277965001, ROCHE) enhanced by Bluing reagent (05266769001, ROCHE) and mounted with xylene-based mounting medium (Sakura TissuTek Prisma, Sakura Finetek Europe B.V., The Netherlands). IHC slides were then digitized with a Panoramic 250 Flash II digital microscope (3DHISTECH, Budapest, Hungary) equipped with a Zeiss Plan-Apochromat 20x NA 0.8 objective and a CIS VCC-FC60FR19CL 4 megapixels CMOS sensor (unit cell size 5.5 x 5.5) mounted on a 1.6x optical adaptor, to achieve a scan resolution of 0.24 μ m/pixel in the final whole slide image. A set of twenty-four whole-slide images from the clinical cohort was assembled for training and testing, including twelve images from each clinical site (Institut Universitaire du Cancer de Toulouse and Centre

Hospitalier Universitaire de Bordeaux). Images were allocated in a randomized fashion into the training ($n = 12$) and testing ($n = 12$) cohorts prior to analysis.

References

1. Barisoni, L., et al., *Digital pathology and computational image analysis in nephropathology*. Nat Rev Nephrol, 2020. **16**(11): p. 669-685.
2. Esteva, A., et al., *Deep learning-enabled medical computer vision*. NPJ Digit Med, 2021. **4**(1): p. 5.
3. Deng, S., et al., *Deep learning in digital pathology image analysis: a survey*. Front Med, 2020. **14**(4): p. 470-487.
4. LeCun, Y., Y. Bengio, and G. Hinton, *Deep learning*. Nature, 2015. **521**(7553): p. 436-44.
5. Rudin, C., *Stop Explaining Black Box Machine Learning Models for High Stakes Decisions and Use Interpretable Models Instead*. Nat Mach Intell, 2019. **1**(5): p. 206-215.
6. Gunning, D., *Explainable Artificial Intelligence (XAI)* 2017, DARPA.
7. Banzhaf, W., et al., *Genetic Programming: An Introduction on the Automatic Evolution of computer programs and its Applications*. 1998.
8. Miller, J.F., *Cartesian genetic programming*. Natural computing series. 2011, Berlin, Germany: Springer. 346.
9. Miller, J.F., D. Job, and V.K. Vassilev, *Principles in the Evolutionary Design of Digital Circuits—Part I. Genetic Programming and Evolvable Machines*, 2000. **1**(1): p. 7-35.
10. Miller, J.F. *An empirical study of the efficiency of learning boolean functions using a cartesian genetic programming approach*. in *Proceedings of the genetic and evolutionary computation conference*. 1999.
11. Leitner, J., et al., *Mars Terrain Image Classification using Cartesian Genetic Programming*. 2012.
12. Harding, S., J. Leitner, and J. Schmidhuber, *Cartesian Genetic Programming for Image Processing (CGP-IP)* in *Genetic Programming Theory and Practice X*, R. Riolo, et al., Editors. 2013, Springer. p. 31-44.
13. Miller, J.F., *Cartesian genetic programming: its status and future*. Genetic Programming and Evolvable Machines, 2020. **21**(1): p. 129-168.
14. Wilson, D.G., et al. *Evolving simple programs for playing atari games*. ACM.
15. Ahmad, A., et al. *Breast cancer detection using Cartesian genetic programming evolved artificial neural networks*. in *GECCO'12*. 2012.
16. Suganuma, M., S. Shirakawa, and T. Nagao, *Designing Convolutional Neural Network Architectures Using Cartesian Genetic Programming*, in *Deep Neural Evolution 2020*, Springer.
17. Sekanina, L., et al., *Image Processing and CGP*, in *Cartesian Genetic Programming*, J.F. Miller, Editor. 2011, Springer Berlin Heidelberg: Berlin, Heidelberg. p. 181-215.
18. Beucher, S. and F. Meyer, *The Morphological Approach to Segmentation: The Watershed Transformation*, in *Mathematical Morphology in Image Processing*. 2018, CRC Press. p. 433-481.
19. Serge, B., *IMAGE SEGMENTATION AND MATHEMATICAL MORPHOLOGY*, in <https://people.cmm.minesparis.psl.eu/users/beucher/wtshed.html>.

20. Yuen, H., et al., *Comparative study of Hough Transform methods for circle finding*. Image and Vision Computing, 1990. **8**(1): p. 71-77.
21. Stringer, C., et al., *Cellpose: a generalist algorithm for cellular segmentation*. Nat Methods, 2021. **18**(1): p. 100-106.
22. Schmidt, U., et al., *Cell Detection with Star-Convex Polygons*. 2018, Springer International Publishing. p. 265-273.
23. He, K., et al. *Mask r-cnn*. in *Proceedings of the IEEE international conference on computer vision*. 2017.
24. Graham, S., et al., *HoVer-Net: Simultaneous Segmentation and Classification of Nuclei in Multi-Tissue Histology Images*. 2018.
25. Yang, L., et al., *NuSeT: A deep learning tool for reliably separating and analyzing crowded cells*. PLoS computational biology, 2020. **16**: p. e1008193-e1008193.
26. Weimiao Yu, H.K.L.S.H.W.Y.B.S.A., *CIL_40217, Mus musculus, Neuroblastoma*. 2012, CIL.
27. Bertrand, F., et al., *An initial and rapid step of lytic granule secretion precedes microtubule organizing center polarization at the cytotoxic T lymphocyte/target cell synapse*. Proc Natl Acad Sci U S A, 2013. **110**(15): p. 6073-8.
28. Stinchcombe, J.C., et al., *The immunological synapse of CTL contains a secretory domain and membrane bridges*. Immunity, 2001. **15**(5): p. 751-61.
29. Chang, H.F., et al., *Identification of distinct cytotoxic granules as the origin of supramolecular attack particles in T lymphocytes*. Nat Commun, 2022. **13**(1): p. 1029.
30. Balint, S., et al., *Supramolecular attack particles are autonomous killing entities released from cytotoxic T cells*. Science, 2020. **368**(6493): p. 897-901.
31. McInnes, L., J. Healy, and J. Melville, *Umap: Uniform manifold approximation and projection for dimension reduction*. arXiv preprint arXiv:1802.03426, 2018.
32. Wold, S., K. Esbensen, and P. Geladi, *Principal component analysis*. Chemometrics and intelligent laboratory systems, 1987. **2**(1-3): p. 37-52.
33. Pedregosa, F., et al., *Scikit-learn: Machine Learning in Python*. Journal of Machine Learning Research, 2011. **12**: p. 2825-2830.
34. Filali, L., et al., *Ultrarapid lytic granule release from CTLs activates Ca(2+)-dependent synaptic resistance pathways in melanoma cells*. Sci Adv, 2022. **8**(7): p. eabk3234.
35. Shamaï, G., et al., *Deep learning-based image analysis predicts PD-L1 status from H&E-stained histopathology images in breast cancer*. Nat Commun, 2022. **13**(1): p. 6753.
36. Koelzer, V.H., et al., *Digital image analysis improves precision of PD-L1 scoring in cutaneous melanoma*. Histopathology, 2018. **73**(3): p. 397-406.
37. *Proposal for a REGULATION OF THE EUROPEAN PARLIAMENT AND OF THE COUNCIL LAYING DOWN HARMONISED RULES ON ARTIFICIAL INTELLIGENCE (ARTIFICIAL INTELLIGENCE ACT) 2021*, European Commission Brussels.
38. Blank, J. and K. Deb, *Pymoo: Multi-Objective Optimization in Python*. IEEE Access, 2020. **8**: p. 89497-89509.
39. Deb, K., *Multi-Objective Optimization using Evolutionary Algorithms*. 2001, New York Wiley.

40. Deb, K., et al., *A fast and elitist multiobjective genetic algorithm: NSGA-II*. IEEE Trans. Evol. Comput., 2002. **6**: p. 182-197.
41. Gerules, G. and C. Janikow, *A survey of modularity in genetic programming*, in *2016 IEEE Congress on Evolutionary Computation (CEC)*. 2016. p. 5034–5043.
42. Harding, S., et al., *MT-CGP: Mixed Type Cartesian Genetic Programming*, in *GECCO'12*. 2012: Philadelphia.
43. Zuba-Surma, E.K. and M.Z. Ratajczak, *Analytical capabilities of the ImageStream cytometer*. Methods Cell Biol, 2011. **102**: p. 207-30.
44. Van Rossum, G. and F.L. Drake, *Python 3 Reference Manual*. 2009, Scotts Valley, CA: CreateSpace.
45. Harris, C.R., et al., *Array programming with NumPy*. Nature, 2020. **585**(7825): p. 357-362.
46. Bradski, G., *The OpenCV Library*. Dr. Dobb's Journal of Software Tools, 2000.
47. Van der Walt, S., et al., *scikit-image: image processing in Python*. PeerJ, 2014. **2**: p. e453.
48. Hunter, J.D., *Matplotlib: A 2D graphics environment*. Computing in Science & Engineering, 2007. **9**(3): p. 90-95.
49. Waskom, M.L., *seaborn: statistical data visualization*. Journal of Open Source Software, 2021. **6**(60): p. 3021.
50. Schindelin, J., et al., *Fiji: an open-source platform for biological-image analysis*. Nature Methods, 2012. **9**(7): p. 676-682.
51. Goldman, B. and W. Punch. *Length bias and search limitations in cartesian genetic programming*. in *GECCO '13*. 2013.
52. Hanson, B., et al., *Extracellular vesicle-mediated promotion of myogenic differentiation is dependent on dose, collection media composition, and isolation method*. bioRxiv, 2022: p. 2022.08.22.504734.
53. Coenen-Stass, A.M.L., et al., *Extracellular microRNAs exhibit sequence-dependent stability and cellular release kinetics*. RNA Biol, 2019. **16**(5): p. 696-706.

Acknowledgements

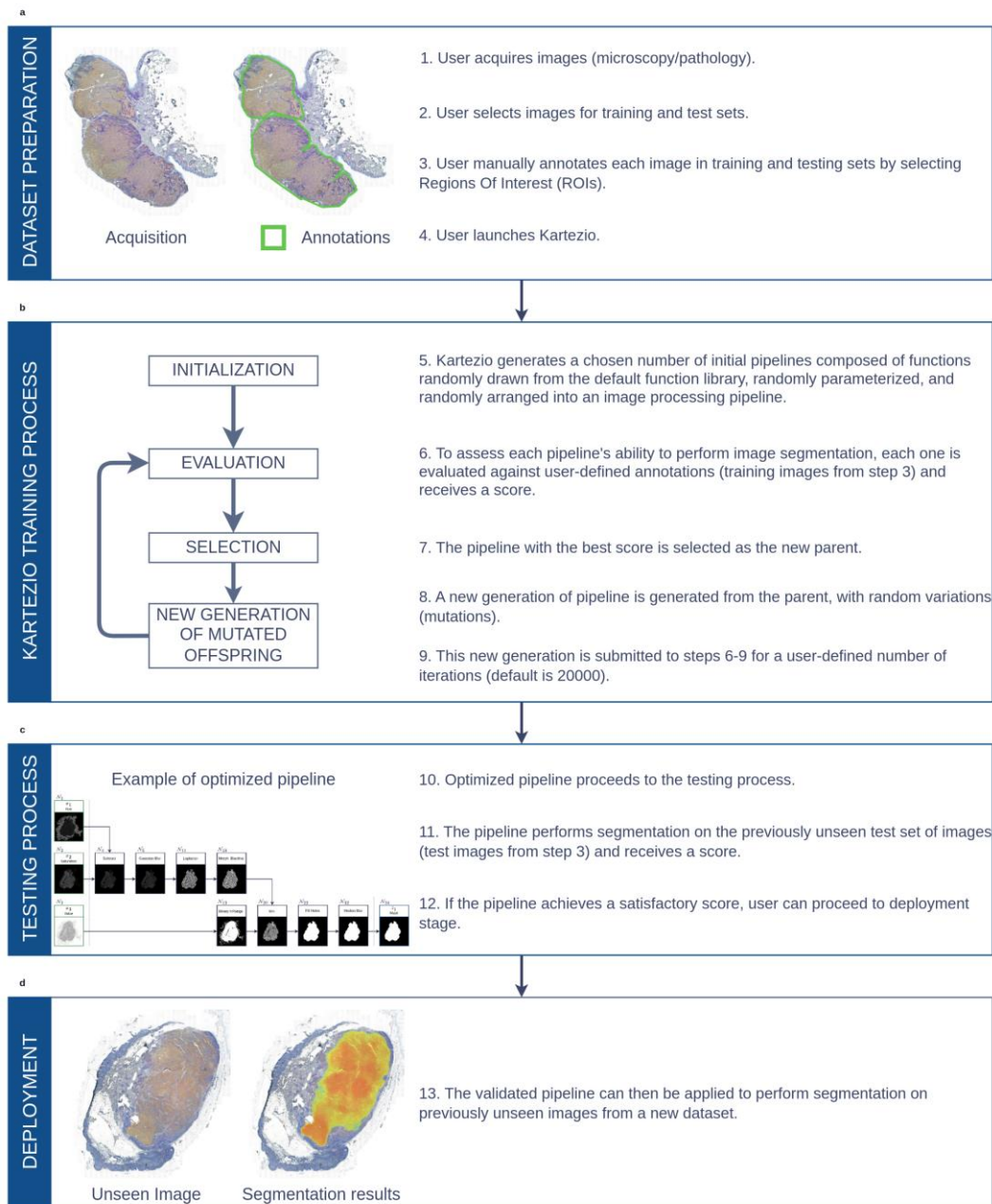
This research has received funding from the European Research Council (ERC) under the European Union's Horizon 2020 Research and Innovation Programme (Grant agreement No. Syn- 951329). This work was performed using HPC resources of the CALMIP supercomputing center under the allocation 2022-[P16043]. This work was supported by the AI Interdisciplinary Institute ANITI, funded by the French program “Investing for the Future – PIA3” under Grant agreement no. ANR-19-PI3A-0004. This work was also supported by grants from the Laboratoire d'Excellence Toulouse Cancer (TOUCAN) (contract ANR11-LABEX). KC was supported by CARE – Graduate School N°ANR-18-EURE-0003, managed by the Agence Nationale de la Recherche under the Programme Investissements d'Avenir. OS was supported by UK Research and Innovation/Marie Sklodowska Curie Actions (Grant number EP/X023907/1). The funders had no role in preparation of the manuscript.

Data & Code Availability

All relevant datasets, genomes, and model history will be archived and accessible on the IRIT institutional server. Source code will be available for non-commercial use on GitHub and on the IRIT institutional server.

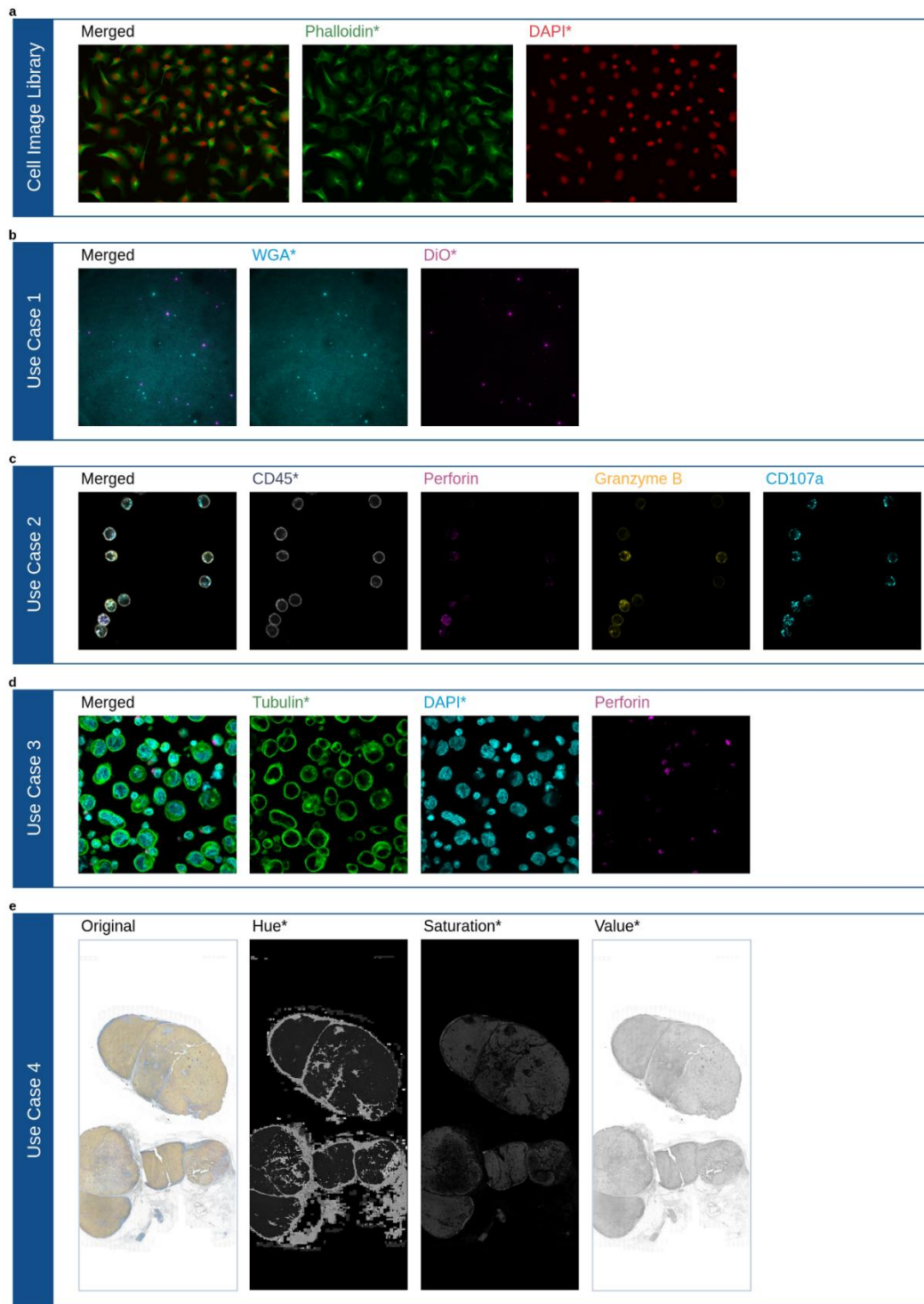
Competing Interests

The following patent application has been filed by KC, SV, SCB, DW, HL, and BM.: “**K. Cortacero *et al.* filed patent; EP 22307041.8**”. The authors declare that they have no other competing interests.



Extended Data Fig. 1 | Conceptual summary of Kartezio

(a) Dataset preparation by experimentalist; (b) illustration of Kartezio training; (c) illustration of Kartezio testing; (d) deployment of Kartezio-generated pipeline.



Extended Data Fig. 2 | Illustrative images from each Use Case

(a) Images from the previously published cell image library [21, 26] (described in **Fig. 2**) wherein *in vitro* neurons were stained with phalloidin (green) and DAPI (red) (b) **Use Case 1**: Extracellular particles derived from polyclonal CTLs (shown in **Fig. 3**) were stained with WGA (cyan) and DiO (magenta) and imaged using TIRFM. (c) **Use Case 2**: Human polyclonal CD8⁺ CTLs (see **Fig. 4**) were stained with antibodies directed against CD45 (gray), perforin (magenta), granzyme B (yellow) and CD107a (cyan). (d) **Use Case 3**: A mixed population of cells containing both human clonal CTLs and target cells (**Fig. 5**) was stained with DAPI (cyan) and antibodies directed against α -tubulin (green) and perforin (magenta). (e) **Use Case 4**: Melanoma nodule datasets (**Fig. 6**) comprised of fixed tissue slices were stained for Sox10 (orange), CD8 (purple), CD107a (black) and counterstained with hematoxylin (blue). Original images were split into Hue, Saturation, and Value channels as shown for analysis. * indicates channel was used as a model input for the corresponding Use Case.

a

```

class ModelWGA(CodeModel):
    def __init__(self):
        super().__init__(endpoint=LocalMaxWatershed(**{'threshold': 1, 'markers_distance': 5}))
    def _parse(self, X):
        x_0 = X[0]
        node_1 = self.call_node("morph_tophat", [x_0], [82, 174])
        node_2 = self.call_node("close", [node_1], [98, 97])
        node_5 = self.call_node("canny", [node_2], [141, 73])
        node_15 = self.call_node("sharpen", [x_0], [195, 116])
        node_16 = self.call_node("subtract", [node_5, node_15], [36, 133])
        node_18 = self.call_node("laplacian", [node_16], [122, 18])
        node_19 = self.call_node("fill_holes", [node_18], [235, 133])
        y_0 = node_19
        Y = [y_0]
        return Y

```

b

```

class ModelDiO(CodeModel):
    def __init__(self):
        super().__init__(endpoint=LocalMaxWatershed(**{'threshold': 1, 'markers_distance': 5}))
    def _parse(self, X):
        x_0 = X[0]
        node_1 = self.call_node("canny", [x_0], [33, 69])
        node_3 = self.call_node("mean", [x_0, node_1], [175, 167])
        node_9 = self.call_node("canny", [node_3], [123, 44])
        node_12 = self.call_node("laplacian", [x_0], [207, 243])
        node_13 = self.call_node("sobel", [node_12], [65, 207])
        node_17 = self.call_node("close", [node_9], [25, 178])
        node_28 = self.call_node("bitwise_and_mask", [node_13, node_17], [227, 124])
        y_0 = node_28
        Y = [y_0]
        return Y

```

Extended Data Fig. 3 | Automatically generated Python classes by Kartezio from given genomes

Panels show the 2 classes, one for WGA **(a)** and one for DiO **(b)** that have been used for the Use Case 1 analysis depicted in **Figure 3**.

Extended Data Table 1 | Functions included in the default library L accessible by Kartezio

Function	Index	Symbol	Arity	Parameters	Sources
max	0	MAX	2	0	OpenCV
min	1	MIN	2	0	OpenCV
mean	2	MEAN	2	0	OpenCV
add	3	ADD	2	0	OpenCV
subtract	4	SUB	2	0	OpenCV
bitwise_not	5	NOT	1	0	OpenCV
bitwise_or	6	BOR	2	0	OpenCV
bitwise_and	7	BAND	2	0	OpenCV
bitwise_and_mask	8	ANDM	2	0	OpenCV
bitwise_xor	9	BXOR	2	0	OpenCV
sqrt	10	SQRT	1	0	OpenCV
pow2	11	POW	1	0	OpenCV
exp	12	EXP	1	0	OpenCV
log	13	LOG	1	0	Numpy
median_blur	14	BLRM	1	1	OpenCV
gaussian_blur	15	BLRG	1	1	OpenCV
laplacian	16	LPLC	1	0	OpenCV
sobel	17	SOBL	1	2	OpenCV
robert_cross	18	RBRT	1	1	OpenCV
canny	19	CANY	1	2	OpenCV
sharpen	20	SHRP	1	0	OpenCV
gabor	21	GABR	1	2	OpenCV
abs_diff	22	ABSD	1	2	OpenCV
abs_diff2	23	ABS2	2	0	OpenCV
fluo_tophat	24	FLUO	1	2	Handmade
rel_diff	25	RELD	1	1	Handmade
erode	26	EROD	1	2	OpenCV
dilate	27	DILT	1	2	OpenCV
open	28	OPEN	1	2	OpenCV
close	29	CLSE	1	2	OpenCV
morph_gradient	30	MGRD	1	2	OpenCV
morph_tophat	31	MTHT	1	2	OpenCV
morph_blackhat	32	MBHT	1	2	OpenCV
fill_holes	33	FILL	1	0	Handmade
remove_small_objects	34	RMSO	1	1	Skimage
remove_small_holes	35	RMSH	1	1	Skimage
threshold	36	TRH	1	2	OpenCV
threshold_at_1	37	TRH1	1	1	OpenCV
distance_transform	38	DTRF	1	1	OpenCV
dt_and_thresh	39	DTTR	1	2	OpenCV
inrange_bin	40	BRNG	1	2	OpenCV
inrange	41	RNG	1	2	OpenCV

Extended Data Table 2 | Fitness scores achieved by Kartezio with descending numbers of training images

Training Images	Median Training ROIs	Training Fitness	Test Images	Test ROIs	Test Fitness
89	4701	0.853 \pm 0.016	11	521	0.858 \pm 0.020
50	2629	0.857 \pm 0.015	11	521	0.849 \pm 0.026
25	1306	0.860 \pm 0.021	11	521	0.840 \pm 0.025
20	1022	0.855 \pm 0.020	11	521	0.843 \pm 0.023
15	771	0.867 \pm 0.028	11	521	0.844 \pm 0.025
14	698	0.864 \pm 0.024	11	521	0.837 \pm 0.032
13	713	0.873 \pm 0.028	11	521	0.832 \pm 0.031
12	632	0.876 \pm 0.028	11	521	0.828 \pm 0.023
11	583	0.865 \pm 0.031	11	521	0.828 \pm 0.036
10	510	0.869 \pm 0.030	11	521	0.825 \pm 0.032
9	451	0.872 \pm 0.031	11	521	0.830 \pm 0.033
8	411	0.888 \pm 0.036	11	521	0.828 \pm 0.029
7	382	0.880 \pm 0.042	11	521	0.807 \pm 0.051
6	351	0.882 \pm 0.031	11	521	0.810 \pm 0.054
5	236	0.886 \pm 0.036	11	521	0.798 \pm 0.061
4	172	0.890 \pm 0.035	11	521	0.790 \pm 0.066
3	160	0.895 \pm 0.044	11	521	0.767 \pm 0.066
2	96	0.918 \pm 0.044	11	521	0.732 \pm 0.102
1	32	0.933 \pm 0.058	11	521	0.584 \pm 0.135

ROI = region of interest; training fitness scores shown represent the mean \pm SD for n = 35 pipelines

Extended Data Table 3 | Summary of Use Case dataset preparation and analysis

	Use Case 1		Use Case 2	Use Case 3	Use Case 4
Use Case Name	Extracellular Particles (SMAPs)		CTL Lytic Arsenal	Lytic Synapse	Tumor Nodules
Imaging Type	2D IF (TIRF)		3D IF	3D IF	2D IHC
Image Processing Task	Instance Segmentation		Instance Segmentation	Instance Segmentation	Semantic Segmentation
Staining	WGA and DiO probes		CD45, Perforin, Granzyme B and CD107a Abs	α -tubulin and perforin Abs, DAPI probe	Sox10, CD8 and CD107a Abs, hematoxylin dye
Scale	1pixel = 0.107 μ m		1pixel = 0.264 μ m	1pixel = 0.264 μ m	1pixel = 46.8 μ m
Number of Datasets	2		1	1	1
Dataset Name	WGA Particles	DiO Particles	CTL Cells	CTL/Target Cells	Tumor Nodules
Training Images	1 $\xrightarrow{\text{split}}$ 4	1 $\xrightarrow{\text{split}}$ 4	5	8	12
Training ROIs	56	44	45	262	12
Testing Images	1 $\xrightarrow{\text{split}}$ 4	1 $\xrightarrow{\text{split}}$ 4	4	4	12
Testing ROIs	48	31	34	150	12
Post-Segmentation Analysis	Matching between masks using Intersection Over Union metric followed by feature extraction (MFI, particle size)		Feature extraction from instances (MFI) followed by 2D embedding and visualization using UMAP	Unsupervised machine learning classification using Gaussian Mixture Model followed by synapse detection	Heatmap generation from the average of 100 models

CTL = cytotoxic T lymphocyte; **SMAP** = supra-molecular attack particle; **IF** = immunofluorescence; **IHC** = immunohistochemistry; **Abs** = antibodies; **TIRFM** = total internal reflection fluorescence microscopy; **ROI** = region of interest

Extended Data Table 4 | Summary of Use Case model parameterization

	Dimension	Number of Models	Name of Model	Model Inputs	Model Outputs	Aggregation	Model Endpoint
Use Case 1	2D	2	WGA Model	$\iota = 1, \{\text{WGA}\}$	$o = 1$	-	Local-Max Watershed
			DiO Model	$\iota = 1, \{\text{DiO}\}$	$o = 1$	-	Local-Max Watershed
Use Case 2	3D	1	CTL Model	$\iota = 1, \{\text{CD45}\}$	$o = 1$	Average	Local-Max Watershed
Use Case 3	3D	1	Cell Model	$\iota = 2, \{\text{DAPI, Tubulin}\}$	$o = 2$	Average	Watershed
Use Case 4	2D	1	Nodule Model	$\iota = 3, \{\text{Hue, Sat., Val.}\}$	$o = 1$	-	Threshold

CTL = cytotoxic T lymphocyte; **WGA** = wheat germ agglutinin; **Sat** = saturation; **Val** = value

Extended Data Table 5 | Summary of Use Case fitness scores

	Training Min	Training Max	Training Average	Test Min	Test Max	Test Average
Use Case 1 (WGA)	0.658	0.872	0.805 ± 0.038	0.378	0.838	0.733 ± 0.084
Use Case 1 (DiO)	0.713	0.839	0.788 ± 0.030	0.399	0.847	0.762 ± 0.091
Use Case 2	0.796	1.000	0.929 ± 0.064	0.776	0.889	0.825 ± 0.029
Use Case 3	0.729	0.805	0.752 ± 0.025	0.576	0.729	0.666 ± 0.037
Use Case 4	0.840	0.893	0.842 ± 0.039	0.817	0.888	0.819 ± 0.062

WGA = wheat germ agglutinin

Extended Data Movie

Extended Data Movie 1 | An illustrative example of an instance segmentation pipeline iteratively evolving using Kartezio

This is an illustrative example of an instance segmentation pipeline evolving using Kartezio, according to a $1 + \lambda$ evolution strategy wherein $\lambda = 2$. Two training images (denoted *Original Image A* and *Original Image B*) and their corresponding manual annotations (*Annotations A* and *Annotations B*) were selected from the original Cellpose specialist dataset [21, 26] and provided to Kartezio, which generated an initial parent pipeline composed of functions randomly drawn from the default function library, randomly parameterized, and randomly arranged into an image processing pipeline. This parent pipeline and two mutated offspring (*Child 1* and *Child 2*) were evaluated against the user-defined annotations for Image A and B. The best pipeline was selected to proceed through the evolutionary selection process, during which the existing parent pipeline was randomly mutated either through changing the functions, the order in which they were arranged in the pipeline, or their parameters. With each iteration (*generation*), this process was repeated. When a new child pipeline outperformed the parent pipeline, it replaced the parent and the evolutionary process continued for a set number of generations (default = 20,000). Of note, in generation 1, all three graphs (parent and two offspring) are randomly generated, while in each subsequent generation, the offspring are generated by mutating the parent pipeline.